J. Fluid Mech. (2022), *vol*. 953, A16, doi:10.1017/jfm.2022.949

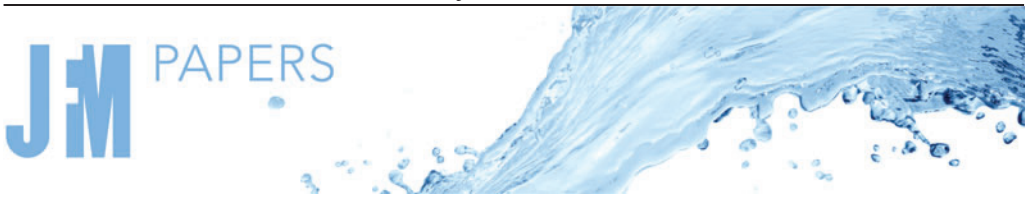

Direct and adjoint problems for sound propagation in non-uniform flows with lined and vibrating surfaces

Sophie Le Bras[1],†, **Gwénaël Gabard**[2] **and Hadrien Bériot**[3]

[1]Siemens Industry Software SAS, 107 Avenue de la République, 92320 Châtillon, France

[2]LAUM (UMR CNRS 6613), Institut d'Acoustique - Graduate School (IA-GS), Le Mans Université, 72085 Le Mans CEDEX 9, France

[3]Siemens Industry Software N.V., Interleuvenlaan 68, 3001 Leuven, Belgium

(Received 22 April 2022; revised 28 October 2022; accepted 6 November 2022)

This paper presents a systematic analysis of direct and adjoint problems for sound propagation with flow. Two scalar propagation operators are considered: the linearised potential equation from Goldstein, and Pierce's equation based on a high-frequency approximation. For both models, the analysis involves compressible base flows, volume sources and surfaces that can be vibrating and/or acoustically lined (using the Myers impedance condition), as well as far-field radiation boundaries. For both models, the direct problems are fully described and adjoint problems are formulated to define tailored Green's functions. These Green's functions are devised to provide an explicit link between the direct problem solutions and the source terms. These adjoint problems and tailored Green's functions are particularly useful and efficient for source localisation problems, or when stochastic distributed sources are involved. The present analysis yields a number of new results, including the adjoint Myers condition for the linearised potential equation, as well as the formulation of the direct and adjoint Myers condition for Pierce's equation. It is also shown how the adjoint problems can be recast in forms that are readily solved using existing simulation tools for the direct problems. Results presented in this paper are obtained using a high-order finite element method. Several test cases serve as validation for the approach using tailored Green's functions. They also illustrate the relative benefits of the two propagation operators.

Key words: aeroacoustics

† Email address for correspondence: sophie.le_bras@siemens.com

1. Introduction

Simulating the propagation of sound in non-uniform mean flows is of interest for many practical applications. Various linearised acoustic operators are available in the literature for this purpose (Astley 2009). Amongst them, the linearised Euler equations (LEE) are attractive as they provide a full description of the refraction of sound waves propagating through sheared mean flows. A major drawback remains the computational cost associated to their resolution in both the time domain and the frequency domain. Another shortcoming is the presence of hydrodynamic instabilities, which can be difficult to handle as they can swamp the acoustic field. In order to prevent the exponential growth of hydrodynamic instabilities, a family of acoustic perturbation equations has been developed by Ewert & Schröder (2003). They are derived from the LEE by excluding non-acoustic modes, but can still be costly to solve.

Various scalar linearised acoustic operators can be considered to reduce the computational costs. For instance, the well-known linearised potential equation proposed by Blokhintzev (1946) and Goldstein (1978) constitutes an efficient way to model sound propagation in potential mean flows (Hamiche *et al.* 2019). It is written for the acoustic velocity potential assuming that both vorticity and entropy effects are excluded from the mean flow and the linear perturbations. Alternatively, Pierce (1990) proposed a scalar propagation model based on a high-frequency approximation that can be applied to arbitrary steady base flows.

These propagation models can be solved directly, in either the frequency or the time domain, for a specific geometry, mean flow and source distribution. In many cases it is advantageous to solve the direct problem through the use of a tailored adjoint Green's function, which is itself a solution of an adjoint problem. Tailored adjoint Green's functions are independent of the source distribution but are functions of the observer position. They represent the transfer functions between any source distribution and the solution at a single observer location. A specific solution is obtained by a simple scalar product between the Green's function and the given source distribution, which is computationally efficient. This is useful when one has to consider many different source distributions for a limited number of observer positions. It is also particularly efficient when dealing with stochastic sources or for source localisation problems. The use of adjoint problems and tailored Green's functions has proved invaluable to solve acoustic analogies, either for self-noise from turbulence (Tam & Auriault 1998) or for interaction noise (Schram 2009). A review of the adjoint-based methods for sound propagation with flow can be found in Spieser & Bailly (2020). Note that previous work considered free-field propagation or involved only rigid scatterers.

The present work provides a systematic analysis of direct and adjoint problems for sound propagation with flow based on Goldstein's and Pierce's wave equations. For both propagation models, the analysis involves compressible base flows, volume sources and surfaces that can be vibrating and/or acoustically lined, as well as far-field radiation boundaries. The coupling between the liner and the acoustic waves is modelled by the Myers impedance condition (Myers 1980) assuming the presence of an infinitely thin boundary layer above the liner. For both models, the direct problems are fully described and adjoint problems are formulated to define tailored Green's functions. These Green's functions are devised to provide an explicit link between the direct problem solutions and the source terms (volume source and surface vibration). A number of new results are reported, including the adjoint Myers condition for Goldstein's equation, as well as the formulation of the direct and adjoint Myers condition for Pierce's equation. We also examine how the adjoint problems can be recast in forms that are readily solved using

existing simulation tools for the direct problems. Several test cases serve as validation for the approach using tailored adjoint Green's functions. They also illustrate the relative benefits of the two propagation operators compared to the LEE.

Tailored Green's functions have initially been devised for analytical modelling (Howe 2003), but closed-form expressions exist only for canonical geometries. They can also be obtained numerically, by solving the adjoint problem for each observer position. For this purpose, the boundary element method has been used to solve the classical Helmholtz equation (Schram 2009; Chaillat *et al.* 2022) or the convected Helmholtz equation (Hu, Guo & Jones 2005). In the present work, the direct and adjoint problems are solved in the frequency domain using a high-order finite element method that has been applied previously to solve propagation problems based on the Helmholtz equation (Bériot, Prinn & Gabard 2016), Goldstein's equation (Gabard *et al.* 2018) and the LEE (Hamiche *et al.* 2019).

The paper is organised as follows. Sections 2 and 3 consider Goldstein's and Pierce's equations, respectively, with each section discussing in details the formulation of the direct and adjoint problems. Section 4 describes how the adjoint problems can be solved efficiently using existing methods. In § 5, several test cases are presented to validate the theoretical developments from §§ 2 and 3. The relative performance of Pierce's and Goldstein's wave operators in the presence of non-isothermal sheared flows is also assessed.

2. Goldstein's equation

We begin with the well-known propagation model for sound waves in a potential base flow derived by Goldstein (1978); see also Blokhintzev (1946). Both the steady base flow and the linear perturbations are assumed to derive from velocity potentials and to be homentropic, hence excluding vorticity waves and entropy waves.

2.1. *Direct problem*

2.1.1. *Governing equation*

Goldstein (1978) derived the following scalar wave equation for the perturbation ϕ of the velocity potential:

$$\rho_0 \frac{\mathrm{d}_0}{\mathrm{d}t}\left(\frac{1}{c_0^2}\frac{\mathrm{d}_0\phi}{\mathrm{d}t}\right) - \boldsymbol{\nabla}\cdot(\rho_0\,\boldsymbol{\nabla}\phi) = -q, \tag{2.1}$$

where $\mathrm{d}_0/\mathrm{d}t = \partial/\partial t + \boldsymbol{u}_0\cdot\boldsymbol{\nabla}$ is the material derivative with respect to the mean flow velocity $\boldsymbol{u}_0$, c_0 is the speed of sound, ρ_0 is the mean flow density, and q is a generic distributed source. From the potential ϕ, it is possible to compute the other acoustic quantities such as pressure, density and velocity:

$$p = -\rho_0\frac{\mathrm{d}_0\phi}{\mathrm{d}t}, \quad \rho = p/c_0^2, \quad \boldsymbol{u} = \boldsymbol{\nabla}\phi. \tag{2.2a–c}$$

This model is solved in the frequency domain using the implicit time dependence $\mathrm{e}^{+\mathrm{i}\omega t}$. This amounts to replacing the material derivative $\mathrm{d}_0/\mathrm{d}t$ in the above expressions by its frequency-domain counterpart $\mathrm{D}_0/\mathrm{D}t = \mathrm{i}\omega + \boldsymbol{u}_0\cdot\boldsymbol{\nabla}$.

2.1.2. *Variational formulation*

For a domain Ω with boundary $\partial\Omega$, the variational formulation for (2.1) reads

$$\int_\Omega \left(\rho_0 \nabla\bar{\psi} \cdot \nabla\phi - \frac{\rho_0}{c_0^2} \overline{\frac{\mathrm{D}_0\psi}{\mathrm{D}t}} \frac{\mathrm{D}_0\phi}{\mathrm{D}t} \right) \mathrm{d}\Omega + \int_{\partial\Omega} \rho_0\bar{\psi} \left(\frac{\boldsymbol{u}_0 \cdot \boldsymbol{n}}{c_0^2} \frac{\mathrm{D}_0\phi}{\mathrm{D}t} - \frac{\partial\phi}{\partial n} \right) \mathrm{d}\Gamma = -\int_\Omega \bar{\psi} q \, \mathrm{d}\Omega, \tag{2.3}$$

where ψ is the test function associated with the velocity potential ϕ, $\bar{\cdot}$ is the complex conjugate, and $\boldsymbol{n}$ is the unit outward normal vector on $\partial\Omega$.

The boundary integral in (2.3) should be investigated to consider each different boundary condition. In this paper, we will consider two types of boundary conditions: a lined and vibrating surface denoted Γ, and a radiation condition imposed on a boundary Γ_∞ located in the far field. We now describe in detail these two boundary conditions.

2.1.3. *Boundary condition for a lined and vibrating surface*

The boundary Γ is a lined and vibrating surface with acoustic admittance A and a prescribed normal velocity v_s. It is also assumed impervious to the mean flow, therefore $\boldsymbol{u}_0 \cdot \boldsymbol{n} = 0$. The corresponding boundary integral in the variational formulation (2.3) is

$$I_\Gamma = -\int_\Gamma \rho_0\bar{\psi} \frac{\partial\phi}{\partial n} \mathrm{d}\Gamma. \tag{2.4}$$

Due to the grazing mean flow, the presence of the acoustic treatment on the surface is accounted for with the Myers (1980) condition, which assumes an infinitely thin boundary layer above the surface. It relates the normal fluctuating velocity $\boldsymbol{u} \cdot \boldsymbol{n}$ of the fluid above the boundary layer to the normal displacement ξ of the fluid on the surface:

$$\boldsymbol{u} \cdot \boldsymbol{n} = \frac{\mathrm{D}_0\xi}{\mathrm{D}t} - \xi \boldsymbol{n} \cdot [(\boldsymbol{n} \cdot \nabla)\boldsymbol{u}_0], \tag{2.5}$$

where $\mathrm{i}\omega\xi$ is the total normal velocity of the surface defined as a combination of the prescribed normal velocity v_s and the relative fluid velocity Ap through the surface allowed by the acoustic treatment, i.e.

$$\mathrm{i}\omega\xi = v_s + Ap. \tag{2.6}$$

Upon introducing the Myers condition (2.5), the boundary term (2.4) becomes

$$I_\Gamma = -\int_\Gamma \rho_0\bar{\psi} \left\{ \frac{\mathrm{D}_0\xi}{\mathrm{D}t} - \xi \boldsymbol{n} \cdot [(\boldsymbol{n} \cdot \nabla)\boldsymbol{u}_0] \right\} \mathrm{d}\Gamma. \tag{2.7}$$

Eversman (2001*a*) shows that this integral can be simplified by using the following result from vector analysis (see also Möhring 2001),

$$\rho_0\bar{\psi}\xi \boldsymbol{n} \cdot [(\boldsymbol{n} \cdot \nabla)\boldsymbol{u}_0] = \nabla \cdot (\rho_0\bar{\psi}\xi\boldsymbol{u}_0) - \boldsymbol{n} \cdot [\nabla \times (\boldsymbol{n} \times \rho_0\bar{\psi}\xi\boldsymbol{u}_0)], \tag{2.8}$$

together with Stokes' theorem. This yields the following expression for the boundary integral:

$$I_\Gamma = \int_\Gamma \rho_0 \overline{\frac{\mathrm{D}_0\psi}{\mathrm{D}t}} \xi \, \mathrm{d}\Gamma + \oint_{\partial\Gamma} \rho_0\bar{\psi}\xi(\boldsymbol{u_0} \times \boldsymbol{n}) \cdot \mathrm{d}\boldsymbol{l}, \tag{2.9}$$

which involves a line integral along the contour of the boundary Γ. Following Eversman (2001*a*) and Rienstra (2007), it can be argued that the normal displacement ξ should

be continuous between a lined surface and a rigid surface (to ensure the continuity of the unsteady streamlines). The displacement should therefore vanish on the contour $\partial\Gamma$, and the contour integral can be removed. In the present case, this implies that both the admittance A and the velocity v_s should vanish on the contour of the surface Γ. With these assumptions, the contour integral along $\partial\Gamma$ is dropped in what follows. Note that this has an impact on the solution, mostly in the vicinity of the liner discontinuity and on the reflection coefficient (Gabard 2010).

After using (2.5) and (2.2*a–c*), the boundary integral for a lined vibrating surface finally reads

$$I_\Gamma = \int_\Gamma \frac{\rho_0}{\mathrm{i}\omega}\,\overline{\frac{\mathrm{D}_0\psi}{\mathrm{D}t}}\,v_s\,\mathrm{d}\Gamma - \int_\Gamma \frac{\rho_0^2 A}{\mathrm{i}\omega}\,\overline{\frac{\mathrm{D}_0\psi}{\mathrm{D}t}}\,\frac{\mathrm{D}_0\phi}{\mathrm{D}t}\,\mathrm{d}\Gamma. \tag{2.10}$$

The first integral is a forcing term that will appear on the right-hand side of the discretised system.

2.1.4. *Far-field radiation condition*

We now consider an outer surface Γ_∞ located far away from the other surfaces and the volume sources. The contribution from this surface to the variational formulation is

$$I_{\Gamma_\infty} = \int_{\Gamma_\infty} \rho_0\bar{\psi}\left(\frac{\boldsymbol{u}_0\cdot\boldsymbol{n}}{c_0^2}\,\frac{\mathrm{D}_0\phi}{\mathrm{D}t} - \frac{\partial\phi}{\partial n}\right)\mathrm{d}\Gamma. \tag{2.11}$$

Without loss of generality, Γ_∞ is chosen as the sphere defined by $\|\boldsymbol{x}\| = r$, hence $\boldsymbol{n} = \boldsymbol{x}/r$ and $\partial/\partial n = \partial/\partial r$.

For the Helmholtz equation (i.e. with no mean flow), one is left with $\partial\phi/\partial r$ on this outer boundary, and the Sommerfeld radiation condition states that the asymptotic behaviour of ϕ in the far field is such that $\partial\phi/\partial r = -\mathrm{i}k\phi$ with $k = \omega/c_0$. The Sommerfeld radiation condition can be generalised to include the effect of a mean flow (Bayliss & Turkel 1982; Tam & Webb 1993; Bogey & Bailly 2002). However these radiation conditions are not directly applicable to the variational formulation (2.3). To derive the radiation condition in a form suitable for (2.1), we have to determine the asymptotic behaviour of all the terms in the parentheses in (2.11).

To that end, we consider the sound field radiated in a uniform mean flow by a generic source term $q(\boldsymbol{x})$ on the right-hand side of (2.1). Using Green's formula, the radiated sound field can be written

$$\phi(\boldsymbol{x}) = -\int q(\boldsymbol{y})\,G(\boldsymbol{x}|\boldsymbol{y})\,\mathrm{d}\boldsymbol{y}, \tag{2.12}$$

where the free-field Green's function $G(\boldsymbol{x}|\boldsymbol{y})$ is defined in three dimensions by

$$G(\boldsymbol{x}|\boldsymbol{y}) = \frac{1}{4\pi\tilde{r}}\exp\left\{-\frac{\mathrm{i}k}{\beta^2}\left[\tilde{r} - (\boldsymbol{x}-\boldsymbol{y})\cdot\frac{\boldsymbol{u}_0}{c_0}\right]\right\}, \tag{2.13}$$

with $\beta^2 = 1 - \|\boldsymbol{u}_0\|^2/c_0^2$, and the distance $\tilde{r}$ defined as

$$\tilde{r} = \sqrt{\beta^2\|\boldsymbol{x}-\boldsymbol{y}\|^2 + [(\boldsymbol{x}-\boldsymbol{y})\cdot\boldsymbol{u}_0]^2/c_0^2}. \tag{2.14}$$

Note that this Green's function already satisfies the far-field radiation condition. After some lengthy developments, it is possible to obtain the following result:

$$\frac{\boldsymbol{u}_0\cdot\boldsymbol{n}}{c_0^2}\,\frac{\mathrm{D}_0\,G(\boldsymbol{x}|\boldsymbol{y})}{\mathrm{D}t} - \frac{\partial G(\boldsymbol{x}|\boldsymbol{y})}{\partial n} = \mathrm{i}k\,\frac{r}{\tilde{r}}\left(1 + \frac{\beta^2}{\mathrm{i}k\tilde{r}}\right)\left(1 - \frac{\boldsymbol{x}\cdot\boldsymbol{y}}{r\tilde{r}}\right)G(\boldsymbol{x}|\boldsymbol{y}), \tag{2.15}$$

where the derivatives on the left-hand side operate on the $\boldsymbol{x}$ coordinate. Note that this result is exact and valid for any value of r, i.e. no far-field approximation has been made.

When the observer is in the geometric far field, which is defined by $\|\boldsymbol{x}\| \gg \|\boldsymbol{y}\|$, the term $\boldsymbol{x}\cdot\boldsymbol{y}/(r\tilde{r})$ in (2.15) can be neglected, and $\tilde{r} \simeq \hat{r} = \sqrt{\beta^2\|\boldsymbol{x}\|^2 + (\boldsymbol{x}\cdot\boldsymbol{u}_0)^2/c_0^2}$. From (2.12) and (2.15), it is apparent that the velocity potential satisfies the following radiation condition in the geometric far field:

$$\frac{\boldsymbol{u}_0\cdot\boldsymbol{x}}{c_0^2 r}\frac{\mathrm{D}_0\phi}{\mathrm{D}t} - \frac{\partial\phi}{\partial r} = \mathrm{i}k\,\frac{r}{\hat{r}}\left(1+\frac{\beta^2}{\mathrm{i}k\hat{r}}\right)\phi + O\left(\frac{1}{r^2}\right), \quad \text{when } r\to+\infty. \tag{2.16}$$

In the absence of mean flow, this radiation condition reduces to the standard Sommerfeld condition; see, for instance, § 4.5.4 in Pierce (2019). The corresponding boundary integral in the variational formulation is written

$$I_{\Gamma_\infty} = \int_{\Gamma_\infty} \mathrm{i}k\alpha\rho_0\bar{\psi}\phi\,\mathrm{d}\Gamma, \tag{2.17}$$

where the coefficient α is defined as

$$\alpha = \frac{r}{\hat{r}}\left(1+\frac{\beta^2}{\mathrm{i}k\hat{r}}\right). \tag{2.18}$$

In (2.16), we have kept the leading-order term, but it is also possible to derive higher-order radiation conditions from (2.15); see Givoli (2004).

The corresponding radiation condition for a two-dimensional problem is given in Appendix A.

2.1.5. *Summary*

To summarise, the direct problem for Goldstein's equation is based on the propagation equation (2.1), which includes a compressible, potential mean flow $\boldsymbol{u}_0$ and a volume sound source q. Boundary conditions include surfaces that can be lined and/or vibrating, based on the Myers condition (2.5), as well as the far-field radiation condition (2.16).

The corresponding variational formulation is (2.3), with the boundary terms given in (2.10) and (2.17).

2.2. *The adjoint operator and tailored Green's functions*

As explained above, it can be particularly useful to use a tailored adjoint Green's function to facilitate or accelerate the calculation of solutions to the direct problems, in this case by providing an explicit expression for the acoustic potential ϕ in terms of the sources v_s and q. Such a tailored Green's function is a solution to an adjoint problem that will be devised in this subsection.

We first introduce scalar products between complex-valued functions, on either Ω or Γ, as follows:

$$\langle f, g\rangle_\Omega = \int_\Omega \overline{f(\boldsymbol{y})}\,g(\boldsymbol{y})\,\mathrm{d}\Omega_y \quad \langle f, g\rangle_\Gamma = \int_\Gamma \overline{f(\boldsymbol{y})}\,g(\boldsymbol{y})\,\mathrm{d}\Gamma_y. \tag{2.19a,b}$$

We then form the scalar product of Goldstein's equation (2.1) with a generic Green's function $G_\phi(\boldsymbol{x},\boldsymbol{y})$, which remains to be defined:

$$\int_\Omega \overline{G_\phi}(\boldsymbol{x},\boldsymbol{y})\,\rho_0(\boldsymbol{y})\,\frac{\mathrm{D}_0}{\mathrm{D}t}\left[\frac{1}{c_0^2(\boldsymbol{y})}\,\frac{\mathrm{D}_0}{\mathrm{D}t}\phi(\boldsymbol{y})\right] - \overline{G_\phi}(\boldsymbol{x},\boldsymbol{y})\,\boldsymbol{\nabla}\cdot\left[\rho_0(\boldsymbol{y})\,\boldsymbol{\nabla}\phi(\boldsymbol{y})\right]\mathrm{d}\Omega_y$$
$$= -\int_\Omega \overline{G_\phi}(\boldsymbol{x},\boldsymbol{y})\,q(\boldsymbol{y})\,\mathrm{d}\Omega_y, \tag{2.20}$$

which is valid for any point $\boldsymbol{x}$ located in Ω, where the integrals are performed over $\boldsymbol{y}$. In the following expressions, we will omit the $\boldsymbol{x}$ and $\boldsymbol{y}$ dependence to simplify the notation. However, to avoid ambiguities, note that all quantities are functions of only $\boldsymbol{y}$ except for G_ϕ, and all the derivatives are applied with respect to $\boldsymbol{y}$. Integrating twice by parts the expression above yields

$$\int_\Omega \phi\,\overline{\left[\rho_0\,\frac{\mathrm{D}_0}{\mathrm{D}t}\left(\frac{1}{c_0^2}\,\frac{\mathrm{D}_0 G_\phi}{\mathrm{D}t}\right) - \boldsymbol{\nabla}_y\cdot\left(\rho_0\,\boldsymbol{\nabla}_y G_\phi\right)\right]}\,\mathrm{d}\Omega_y$$
$$+\int_{\partial\Omega}\frac{\rho_0(\boldsymbol{u}_0\cdot\boldsymbol{n})}{c_0^2}\left(\overline{G_\phi}\,\frac{\mathrm{D}_0\phi}{\mathrm{D}t} - \phi\,\overline{\frac{\mathrm{D}_0 G_\phi}{\mathrm{D}t}}\right) + \rho_0\left(\phi\,\frac{\partial\overline{G_\phi}}{\partial n_y} - \overline{G_\phi}\,\frac{\partial\phi}{\partial n_y}\right)\mathrm{d}\Gamma_y$$
$$= -\int_\Omega \overline{G_\phi} q\,\mathrm{d}\Omega_y. \tag{2.21}$$

Subtracting (2.21) and (2.20) yields the integral form of Lagrange's identity, which relates the direct and adjoint operators; see, for instance, § IV.4 in Dennery & Krzywicki (2012). The adjoint operator to Goldstein's equation (2.1) is readily found in the square brackets in (2.21). In this case, the direct and adjoint operators are identical, which is expected since Goldstein's equation is self-adjoint.

2.2.1. *Adjoint equation*

Our aim is now to identify a tailored adjoint Green's function that provides an explicit solution for the direct problem defined in the previous subsection. In other words, we have to select the governing equation and the boundary conditions for G_ϕ so that the velocity potential ϕ can be written explicitly in terms of the source terms q and v_s. Beginning with the governing equation for G_ϕ, we would like the first integral in (2.21) to reduce to $\phi(\boldsymbol{x})$, i.e. G_ϕ should be such that

$$\int_\Omega \phi\,\overline{\left[\rho_0\,\frac{\mathrm{D}_0}{\mathrm{D}t}\left(\frac{1}{c_0^2}\,\frac{\mathrm{D}_0 G_\phi}{\mathrm{D}t}\right) - \boldsymbol{\nabla}_y\cdot\left(\rho_0\,\boldsymbol{\nabla}_y G_\phi\right)\right]}\,\mathrm{d}\Omega_y = \phi(\boldsymbol{x}). \tag{2.22}$$

This can be achieved if G_ϕ is a solution of

$$\rho_0\,\frac{\mathrm{D}_0}{\mathrm{D}t}\left(\frac{1}{c_0^2}\,\frac{\mathrm{D}_0 G_\phi}{\mathrm{D}t}\right) - \boldsymbol{\nabla}_y\cdot\left(\rho_0\,\boldsymbol{\nabla}_y G_\phi\right) = \delta(\boldsymbol{x}-\boldsymbol{y}), \tag{2.23}$$

which shows that G_ϕ is indeed a Green's function for the adjoint operator.

Looking back at (2.21), the solution $\phi(\boldsymbol{x})$ is now given in terms of integrals on Γ and Ω. While the latter depends on only q and G_ϕ, the boundary integral still involves ϕ. In order to obtain an explicit expression for ϕ, we have to choose the boundary conditions for the Green's function so that the boundary integral involves only G_ϕ and v_s.

2.2.2. *Lined vibrating wall*

We first consider the integral on the boundary Γ representing a lined and vibrating surface, as described in § 2.1.3. Since $\boldsymbol{u}_0 \cdot \boldsymbol{n} = 0$ on this surface, the relevant boundary integral in (2.21) is

$$J_\Gamma = \int_\Gamma \rho_0 \left(\phi \frac{\partial \overline{G_\phi}}{\partial n_y} - \overline{G_\phi} \frac{\partial \phi}{\partial n_y} \right) \mathrm{d}\Gamma_y. \tag{2.24}$$

The second term in this integral is the same as in (2.4) with ψ replaced by G_ϕ. Using the same analysis as in § 2.1.3 for the formulation of the Myers boundary condition, one gets

$$J_\Gamma = \int_\Gamma \frac{\rho_0}{\mathrm{i}\omega} \overline{\frac{\mathrm{D}_0 G_\phi}{\mathrm{D}t}} v_s + \rho_0 \phi \frac{\partial \overline{G_\phi}}{\partial n_y} - \frac{\rho_0^2 A}{\mathrm{i}\omega} \overline{\frac{\mathrm{D}_0 G_\phi}{\mathrm{D}t}} \frac{\mathrm{D}_0 \phi}{\mathrm{D}t} \, \mathrm{d}\Gamma. \tag{2.25}$$

To proceed further, we use steps similar to those described in § 2.1.3 for the formulation of the Myers condition: i.e. the derivative in $\mathrm{D}_0\phi/\mathrm{D}t$ is integrated by parts, an expression similar to (2.8) is used, and we apply Stokes' theorem. This yields

$$\begin{aligned} J_\Gamma = {} & \int_\Gamma \frac{\rho_0}{\mathrm{i}\omega} \overline{\frac{\mathrm{D}_0 G_\phi}{\mathrm{D}t}} v_s \, \mathrm{d}\Gamma + \oint_{\partial\Gamma} \phi \frac{\rho_0^2 A}{\mathrm{i}\omega} \overline{\frac{\mathrm{D}_0 G_\phi}{\mathrm{D}t}} (\boldsymbol{u}_0 \times \boldsymbol{n}) \cdot \mathrm{d}\boldsymbol{l} \\ & + \int_\Gamma \rho_0 \phi \overline{\left\{ \frac{\partial G_\phi}{\partial n_y} - \frac{\mathrm{D}_0}{\mathrm{D}t} \left(\frac{\rho_0 \bar{A}}{\mathrm{i}\omega} \frac{\mathrm{D}_0 G_\phi}{\mathrm{D}t} \right) + \frac{\rho_0 \bar{A}}{\mathrm{i}\omega} \frac{\mathrm{D}_0 G_\phi}{\mathrm{D}t} \boldsymbol{n} \cdot [(\boldsymbol{n} \cdot \nabla_y) \boldsymbol{u}_0] \right\}}. \end{aligned} \tag{2.26}$$

Recall that the aim is to remove ϕ from this expression. First, we can use the same argument as in Eversman (2001*a*) for the direct problem: assuming that the admittance A varies continuously on Γ, the contour $\partial\Gamma$ can be located on the rigid wall and the contour integral above vanishes. Second, the last integral in (2.26) is eliminated by choosing the following boundary condition for the tailored adjoint Green's function G_ϕ:

$$\frac{\partial G_\phi}{\partial n_y} = \frac{\mathrm{D}_0 \eta}{\mathrm{D}t} - \eta \boldsymbol{n} \cdot [(\boldsymbol{n} \cdot \nabla_y) \boldsymbol{u}_0], \quad \text{with } \mathrm{i}\omega\eta = \rho_0 \bar{A} \frac{\mathrm{D}_0 G_\phi}{\mathrm{D}t}, \quad \text{on } \Gamma. \tag{2.27}$$

This expression is the adjoint Myers condition. It takes a form similar to the original impedance condition (2.5) for the direct problem except for several important differences. There is a sign difference compared to (2.5), and the admittance A is replaced by its complex conjugate. In addition, the source term v_s does not appear in the adjoint impedance condition (2.27) for the tailored Green's function G_ϕ.

2.2.3. *Radiation condition*

The contribution of the radiation boundary Γ_∞ in (2.21) is

$$J_{\Gamma_\infty} = \int_{\Gamma_\infty} \frac{\rho_0 (\boldsymbol{u}_0 \cdot \boldsymbol{n})}{c_0^2} \left(\overline{G_\phi} \frac{\mathrm{D}_0 \phi}{\mathrm{D}t} - \phi \overline{\frac{\mathrm{D}_0 G_\phi}{\mathrm{D}t}} \right) + \rho_0 \left(\phi \frac{\partial \overline{G_\phi}}{\partial n_y} - \overline{G_\phi} \frac{\partial \phi}{\partial n_y} \right) \mathrm{d}\Gamma_y. \tag{2.28}$$

Using the radiation condition (2.16) satisfied by ϕ on Γ_∞, this contribution becomes

$$J_{\Gamma_\infty} = \int_{\Gamma_\infty} \rho_0 \phi \overline{\left(\frac{\partial G_\phi}{\partial n_y} - \frac{\boldsymbol{u}_0 \cdot \boldsymbol{n}}{c_0^2} \frac{\mathrm{D}_0 G_\phi}{\mathrm{D}t} - \mathrm{i}k\bar{\alpha} G_\phi \right)} \mathrm{d}\Gamma_y, \tag{2.29}$$

with α defined in (2.17). For this contribution to vanish, the Green's function G_ϕ should satisfy the following adjoint radiation condition on Γ_∞:

$$\frac{\boldsymbol{u}_0 \cdot \boldsymbol{y}}{c_0^2 r} \frac{\mathrm{D}_0 G_\phi}{\mathrm{D}t} - \frac{\partial G_\phi}{\partial r} = -\mathrm{i}k\bar{\alpha} G_\phi. \tag{2.30}$$

It is similar to the direct radiation condition (2.16) except that $\mathrm{i}k\alpha$ is replaced by its complex conjugate $-\mathrm{i}k\bar{\alpha}$. This is a consequence of the fact that the adjoint problem is anti-causal. The adjoint radiation condition allows only inward-propagating waves, which is the opposite of the radiation condition for the direct problem, which allows only outward-propagating waves.

2.2.4. *Summary and discussion*

The acoustic potential ϕ can be written explicitly in terms of the source terms v_s and q as

$$\phi(\boldsymbol{x}) = \left\langle -\rho_0 \frac{\mathrm{D}_0 G_\phi}{\mathrm{D}t}, \frac{v_s}{\mathrm{i}\omega} \right\rangle_\Gamma - \langle G_\phi, q \rangle_\Omega = -\int_\Gamma \frac{\rho_0}{\mathrm{i}\omega} \overline{\frac{\mathrm{D}_0 G_\phi}{\mathrm{D}t}}\, v_s \,\mathrm{d}\Gamma_y - \int_\Omega \overline{G_\phi} q \,\mathrm{d}\Omega_y, \tag{2.31}$$

provided that the tailored adjoint Green's function G_ϕ is defined as follows:

$$\left.\begin{aligned} &\rho_0 \frac{\mathrm{D}_0}{\mathrm{D}t}\left(\frac{1}{c_0^2}\frac{\mathrm{D}_0}{\mathrm{D}t} G_\phi\right) - \boldsymbol{\nabla}_y \cdot \left(\rho_0 \boldsymbol{\nabla}_y G_\phi\right) = \delta(\boldsymbol{x}-\boldsymbol{y}) \quad \text{in } \Omega, \\ &\frac{\partial G_\phi}{\partial n_y} = \frac{\mathrm{D}_0 \eta}{\mathrm{D}t} - \eta \boldsymbol{n} \cdot [(\boldsymbol{n} \cdot \boldsymbol{\nabla}_y)\boldsymbol{u}_0] \quad \text{with } \mathrm{i}\omega\eta = \rho_0 \bar{A} \frac{\mathrm{D}_0 G_\phi}{\mathrm{D}t} \quad \text{on } \Gamma, \\ &\frac{\boldsymbol{u}_0 \cdot \boldsymbol{y}}{c_0^2 r} \frac{\mathrm{D}_0 G_\phi}{\mathrm{D}t} - \frac{\partial G_\phi}{\partial r} = -\mathrm{i}k\bar{\alpha} G_\phi \quad \text{on } \Gamma_\infty. \end{aligned}\right\} \tag{2.32}$$

It is worth noting a number of points concerning the direct and adjoint problems.

(i) While the propagation operator is self-adjoint, the boundary conditions are not self-adjoint since they differ between the direct and adjoint problems. The practical implications of these differences will be discussed in § 4.

(ii) The surface admittance A does not appear explicitly in (2.31). It is taken into account implicitly by the tailored Green's function G_ϕ through the adjoint impedance condition (2.27) that it satisfies on the surface Γ.

(iii) In the expression (2.31), it is clear that $\boldsymbol{x}$ represents the observer position while the source position $\boldsymbol{y}$ moves on the surface Γ and in the volume Ω. However, in the definition (2.32) of the tailored adjoint Green's function, the differential equation is written in terms of $\boldsymbol{y}$ (the derivative in the equation and the boundary conditions are applied with respect to $\boldsymbol{y}$ and not $\boldsymbol{x}$). This means that in (2.32), the source position is $\boldsymbol{x}$ and the observer position is $\boldsymbol{y}$, which is the reverse from (2.31). The reciprocity principle appears naturally from the derivation of G_ϕ presented above.

(iv) The tailored adjoint Green's function G_ϕ in (2.31) can be understood as the acoustic transfer function between the volume source q and the velocity potential ϕ at the observer position $\boldsymbol{x}$. Likewise, the quantity $-\rho_0 \mathrm{D}_0 G_\phi / \mathrm{D}t$ is the transfer function between the surface displacement $v_s/(\mathrm{i}\omega)$ and the velocity potential $\phi(\boldsymbol{x})$.

In the analysis above, the tailored adjoint Green's function G_ϕ was devised to yield an explicit expression for the velocity potential. If one wishes to compute the acoustic

pressure instead, then it is possible to compute $p(\boldsymbol{x}) = -\rho_0 \,\mathrm{D}_0\phi/\mathrm{D}t$ (with derivatives with respect to $\boldsymbol{x}$) from (2.31). This can be cumbersome as (2.32) yields G_ϕ as a function of $\boldsymbol{y}$ for a fixed $\boldsymbol{x}$. Instead, it is preferable to define another tailored adjoint Green's function $G_p(\boldsymbol{x}, \boldsymbol{y})$ that relates directly p to the source terms q and v_s through

$$p(\boldsymbol{x}) = \left\langle -\rho_0 \frac{\mathrm{D}_0 G_p}{\mathrm{D}t}, \frac{v_s}{\mathrm{i}\omega} \right\rangle_\Gamma - \left\langle G_p, q \right\rangle_\Omega , \tag{2.33}$$

which has the exact same form as (2.31). This is achieved by modifying the right-hand side of (2.23) so that the integral in (2.22) yields $p(\boldsymbol{x})$; that is, the adjoint equation for G_p reads

$$\rho_0 \frac{\mathrm{D}_0}{\mathrm{D}t}\left(\frac{1}{c_0^2}\frac{\mathrm{D}_0 G_p}{\mathrm{D}t}\right) - \boldsymbol{\nabla}_y \cdot \left(\rho_0 \boldsymbol{\nabla}_y G_p\right) = \rho_0 \frac{\mathrm{D}_0}{\mathrm{D}t}\delta(\boldsymbol{x}-\boldsymbol{y}). \tag{2.34}$$

It is straightforward to show that G_p satisfies the same adjoint boundary conditions as in (2.32). A similar methodology can be used to compute the acoustic velocity field $\boldsymbol{u}$ instead of $\phi(\boldsymbol{x})$.

A final comment is that the generic source term q can be replaced easily by a distribution of dipole sources by writing $q = \boldsymbol{\nabla} \cdot \boldsymbol{f}$, where $\boldsymbol{f}$ is the dipole strength. The additional divergence in (2.31) can be transferred onto the Green's function by integrating by parts to write

$$\phi(\boldsymbol{x}) = -\int_\Gamma \frac{\rho_0}{\mathrm{i}\omega}\overline{\frac{\mathrm{D}_0 G_\phi}{\mathrm{D}t}}\, v_s \,\mathrm{d}\Gamma_y + \int_\Omega \boldsymbol{f} \cdot \boldsymbol{\nabla}_y \overline{G_\phi}\,\mathrm{d}\Omega_y. \tag{2.35}$$

A similar approach can be used for other types of sources, such as a quadrupole distribution.

3. Pierce's equation

Pierce (1990) proposed two propagation models derived in the high-frequency limit for an arbitrary steady base flow. The first equation is in fact the same as Goldstein's model (2.1) with the velocity potential ϕ as variable. Pierce (1990) has thus shown that Goldstein's equation is also valid for arbitrary base flows in the high-frequency limit, and the analysis in § 2.2.1 is therefore also valid in this case. In the present section we will focus on the second model from Pierce (1990), namely (27). Details of the analysis will not be repeated as they are similar to the previous section. We will instead highlight the novel results and the key differences with Goldstein's equation.

3.1. *Direct problem*

Instead of the velocity potential ϕ, Pierce (1990) proposes to use the momentum potential φ, which is such that $p = \mathrm{D}_0\varphi/\mathrm{D}t$ and $\rho_0\boldsymbol{u} = -\boldsymbol{\nabla}\varphi$. In the high-frequency limit, this variable satisfies the propagation equation

$$\boldsymbol{\nabla}\cdot\left(\frac{1}{\rho_0}\boldsymbol{\nabla}\varphi\right) - \rho_0 \frac{\mathrm{D}_0}{\mathrm{D}t}\left(\frac{1}{\rho_0^2 c_0^2}\frac{\mathrm{D}_0\varphi}{\mathrm{D}t}\right) = -q, \tag{3.1}$$

which is valid for an arbitrary steady base flow, i.e. compressible, rotational and not necessarily homentropic. Compared to (27) in Pierce (1990) we have added a generic

source distribution on the right-hand side. For a computational domain Ω with boundary $\partial\Omega$, the variational formulation corresponding to (3.1) reads

$$\int_\Omega \frac{1}{\rho_0}\left(\frac{1}{c_0^2}\overline{\frac{\mathrm{D}_0\psi}{\mathrm{D}t}}\frac{\mathrm{D}_0\varphi}{\mathrm{D}t} - \nabla\bar{\psi}\cdot\nabla\varphi\right)\mathrm{d}\Omega + \int_{\partial\Omega}\frac{\bar{\psi}}{\rho_0}\left(\frac{\partial\varphi}{\partial n} - \frac{\boldsymbol{u}_0\cdot\boldsymbol{n}}{c_0^2}\frac{D_0\varphi}{\mathrm{D}t}\right)\mathrm{d}\Gamma = -\int_\Omega \bar{\psi}q\,\mathrm{d}\Omega, \tag{3.2}$$

with the test function ψ. Like in (2.3) for Goldstein's equation, the volume integral above is Hermitian, which is consistent with the fact that there is an energy conservation principle associated with Pierce's equation (3.1); see § 2.4 in Möhring (1999).

The Myers condition is traditionally used with Goldstein's equation (2.1), but we show here how it can be included in the variational formulation for Pierce's equation. When formulated in terms of the potential φ, the Myers impedance condition (2.5) becomes

$$\frac{\partial\varphi}{\partial n} = -\rho_0\left\{\frac{\mathrm{D}_0\xi}{\mathrm{D}t} - \xi\boldsymbol{n}\cdot[(\boldsymbol{n}\cdot\nabla)\boldsymbol{u}_0]\right\}, \tag{3.3}$$

with

$$\mathrm{i}\omega\xi = v_s + A\frac{\mathrm{D}_0\varphi}{\mathrm{D}t}, \tag{3.4}$$

where ξ is again the normal displacement of the surface. Recalling that $\boldsymbol{u}_0\cdot\boldsymbol{n} = 0$ on Γ, the boundary integral on surface Γ in (3.2) reduces to

$$I_\Gamma = \int_\Gamma \frac{\bar{\psi}}{\rho_0}\frac{\partial\varphi}{\partial n}\,\mathrm{d}\Gamma = -\int_\Gamma \rho_0\left(\frac{\bar{\psi}}{\rho_0}\right)\left\{\frac{\mathrm{D}_0\xi}{\mathrm{D}t} - \xi\boldsymbol{n}\cdot[(\boldsymbol{n}\cdot\nabla)\boldsymbol{u}_0]\right\}\mathrm{d}\Gamma. \tag{3.5}$$

Following the same analysis as in § 2.1.3 (in particular using (2.8) where ψ is replaced by ψ/ρ_0), it is possible to write

$$I_\Gamma = \int_\Gamma \frac{\rho_0}{\mathrm{i}\omega}\overline{\frac{\mathrm{D}_0}{\mathrm{D}t}\left(\frac{\psi}{\rho_0}\right)}v_s\,\mathrm{d}\Gamma + \int_\Gamma \frac{\rho_0 A}{\mathrm{i}\omega}\overline{\frac{\mathrm{D}}{\mathrm{D}t}\left(\frac{\psi}{\rho_0}\right)}\frac{\mathrm{D}\varphi}{\mathrm{D}t}\,\mathrm{d}\Gamma. \tag{3.6}$$

This formulation of the Myers impedance condition for Pierce's propagation equation is consistent with Eversman (2001*a*), i.e. the displacement ξ and admittance A are assumed to vary smoothly between a lined and rigid surfaces. The main difference with (2.10) is the substitution of ψ by ψ/ρ_0, which will be discussed further in § 4.

Concerning the radiation boundary Γ_∞, the analysis of the far-field behaviour of the velocity potential ϕ given in § 2.1.4 also applies to the potential φ. It therefore satisfies the same radiation condition (2.16) as ϕ, and the boundary integral on Γ_∞ in (3.2) becomes

$$I_{\Gamma_\infty} = -\int_{\Gamma_\infty}\mathrm{i}k\alpha\frac{\bar{\psi}\varphi}{\rho_0}\,\mathrm{d}\Gamma. \tag{3.7}$$

3.2. *Adjoint problem*

Pierce's equation (3.1) can also be solved using a tailored adjoint Green's function, following the same approach as described in § 2.2 for Goldstein's equation. One starts

by forming the scalar product between Pierce's equation (3.1) and a Green's function $H_\varphi(\boldsymbol{x}, \boldsymbol{y})$. Integrating by parts twice leads to

$$\begin{aligned}\int_\Omega \varphi \left[\overline{\boldsymbol{\nabla}_y \cdot \left(\frac{1}{\rho_0}\boldsymbol{\nabla}_y H_\varphi\right) - \rho_0 \frac{\mathrm{D}_0}{\mathrm{D}t}\left(\frac{1}{\rho_0^2 c_0^2}\frac{\mathrm{D}_0 H_\varphi}{\mathrm{D}t}\right)}\right] \mathrm{d}\Omega_y \\ + \int_{\partial\Omega} \frac{\boldsymbol{u}_0\cdot\boldsymbol{n}}{\rho_0 c_0^2}\left(\varphi\,\overline{\frac{\mathrm{D}_0 H_\varphi}{\mathrm{D}t}} - \overline{H_\varphi}\frac{\mathrm{D}_0\varphi}{\mathrm{D}t}\right) + \frac{1}{\rho_0}\left(\overline{H_\varphi}\frac{\partial\varphi}{\partial n} - \varphi\frac{\partial\overline{H_\varphi}}{\partial n}\right)\mathrm{d}\Gamma_y \\ = -\int_\Omega \overline{H_\varphi} q\,\mathrm{d}\Omega_y,\end{aligned} \tag{3.8}$$

where the integrals and the derivatives operate on the $\boldsymbol{y}$ coordinate.

Again, the objective is to tailor the Green's function H_φ to obtain an explicit expression for φ in terms of the sources q and v_s. Requiring that the first integral in the above expression reduces to $\varphi(\boldsymbol{x})$ leads to the following adjoint equation for the Green's function:

$$\boldsymbol{\nabla}\cdot\left(\frac{1}{\rho_0}\boldsymbol{\nabla} H_\varphi\right) - \rho_0\frac{\mathrm{D}_0}{\mathrm{D}t}\left(\frac{1}{\rho_0^2 c_0^2}\frac{\mathrm{D}_0 H_\varphi}{\mathrm{D}t}\right) = \delta(\boldsymbol{x}-\boldsymbol{y}), \tag{3.9}$$

where the derivatives are taken with respect to $\boldsymbol{y}$. Comparing with the direct problem (3.1), it is clear that Pierce's equation is self-adjoint.

The boundary conditions for H_φ are now selected to remove φ and its derivatives from the boundary integral in (3.8). For the lined vibrating surface Γ, after using the fact that $\boldsymbol{u}_0\cdot\boldsymbol{n} = 0$ and introducing the Myers condition (3.3) for Pierce's equation, the contribution to the boundary integral becomes

$$I_\Gamma = -\int_\Gamma \overline{H_\varphi}\frac{\mathrm{D}_0\xi}{\mathrm{D}t} - \overline{H_\varphi}\xi\boldsymbol{n}\cdot[(\boldsymbol{n}\cdot\boldsymbol{\nabla})\boldsymbol{u}_0] + \frac{\varphi}{\rho_0}\overline{\frac{\partial H_\varphi}{\partial n}}\,\mathrm{d}\Gamma. \tag{3.10}$$

Following the same reasoning as in § 2.2, this contribution can be written as

$$I_\Gamma = \int_\Gamma \frac{\rho_0 v_s}{\mathrm{i}\omega}\overline{\frac{\mathrm{D}_0 H_\varphi}{\mathrm{D}t}}\,\mathrm{d}\Gamma, \tag{3.11}$$

provided that the tailored Green's function satisfies the following adjoint Myers condition for Pierce's equation:

$$\frac{\partial H_\varphi}{\partial n} = \rho_0^2\left\{\frac{\mathrm{D}_0\nu}{\mathrm{D}t} - \nu\boldsymbol{n}\cdot[(\boldsymbol{n}\cdot\boldsymbol{\nabla})\boldsymbol{u}_0]\right\}, \quad \text{with } \nu = \frac{\bar{A}}{\mathrm{i}\omega}\frac{\mathrm{D}_0}{\mathrm{D}t}\left(\frac{H_\varphi}{\rho_0}\right). \tag{3.12}$$

On the far-field surface Γ_∞, the solution φ satisfies the radiation condition (2.16), and the adjoint radiation condition for H_φ is readily identified as

$$\frac{\boldsymbol{u}_0\cdot\boldsymbol{y}}{c_0^2 r}\frac{\mathrm{D}_0 H_\varphi}{\mathrm{D}t} - \frac{\partial H_\varphi}{\partial r} = -\mathrm{i}k\bar{\alpha}H_\varphi, \tag{3.13}$$

which is the same as (2.30).

As a consequence, the potential φ for an observer $\boldsymbol{x}$ can be written explicitly in terms of the sources v_s and q as

$$\varphi(\boldsymbol{x}) = -\int_\Gamma \frac{\rho_0}{\mathrm{i}\omega}\,\overline{\frac{\mathrm{D}_0 H_\varphi}{\mathrm{D}t}}\,v_s\,\mathrm{d}\Gamma_y - \int_\Omega \overline{H_\varphi}\,q\,\mathrm{d}\Omega_y = -\left\langle \frac{\mathrm{D}_0 H_\varphi}{\mathrm{D}t}, \frac{\rho_0 v_s}{\mathrm{i}\omega}\right\rangle_\Gamma - \langle H_\varphi, q\rangle_\Omega\,, \tag{3.14}$$

provided that the tailored Green's function H_φ satisfies the adjoint problem defined by (3.9), (3.12) and (3.13).

All the comments in § 2.2.4 concerning the adjoint problem for Goldstein's equation also apply here. In particular, if one is interested in computing an acoustic quantity other than φ, then it is possible to modify the right-hand side of (3.9) accordingly. For instance, to obtain an explicit expression for the pressure field similar to (3.14), the required tailored adjoint Green's function H_p satisfies

$$\boldsymbol{\nabla}\cdot\left(\frac{1}{\rho_0}\,\boldsymbol{\nabla} H_p\right) - \rho_0\,\frac{\mathrm{D}_0}{\mathrm{D}t}\left(\frac{1}{\rho_0^2 c_0^2}\,\frac{\mathrm{D}_0 H_p}{\mathrm{D}t}\right) = \overline{\frac{\mathrm{D}_0}{\mathrm{D}t}}\,\delta(\boldsymbol{x}-\boldsymbol{y}), \tag{3.15}$$

where the derivatives apply on the $\boldsymbol{y}$ coordinate. The tailored adjoint Green's function H_p also satisfies the boundary conditions (3.12) and (3.13).

4. Solution procedure

We now discuss the computation of the direct and adjoint problems. A first step is to rewrite the adjoint problems in forms that are closer to the direct problems. Then a high-order finite element method is introduced to solve these differential equations efficiently.

4.1. *Flow reversal theorem*

While the two propagation operators (2.1) and (3.1) considered in this paper are self-adjoint, the associated boundary conditions are not self-adjoint. As shown above, the Myers impedance condition (written in (2.5) and (3.3) for ϕ and φ, respectively) differs in the adjoint problems for the tailored Green's functions (see (2.27) and (3.12) for ϕ and φ, respectively). Similarly, the radiation conditions (2.16) and (2.15) differ between the direct and adjoint problems. This implies that non-reflecting conditions and buffer zones, such as perfectly matched layers, would have to be rewritten specifically for the adjoint problems where the radiation condition is anti-causal. Having to implement separate solvers for the direct and adjoint problems is a hindrance that can be partly avoided.

To that end, one has to reverse the mean flow direction (i.e. substitute $\boldsymbol{u}_0$ by $-\boldsymbol{u}_0$) and take the complex conjugate of the propagation equation and the boundary conditions. For Goldstein's equation, the governing equations (2.32), (2.27) and (2.16) for the tailored adjoint Green's function G_ϕ become

$$\left.\begin{aligned}
&\rho_0\,\frac{\mathrm{D}_0}{\mathrm{D}t}\left(\frac{1}{c_0^2}\,\frac{\mathrm{D}_0\overline{G_\phi}}{\mathrm{D}t}\right) - \boldsymbol{\nabla}\cdot\left(\rho_0\,\boldsymbol{\nabla}\overline{G_\phi}\right) = \delta(\boldsymbol{x}-\boldsymbol{y}) \quad \text{in } \Omega,\\
&\frac{\partial\overline{G_\phi}}{\partial n} = -\frac{\mathrm{D}_0\bar\eta}{\mathrm{D}t} + \bar\eta\,\boldsymbol{n}\cdot[(\boldsymbol{n}\cdot\boldsymbol{\nabla})\boldsymbol{u}_0] \quad \text{with } \bar\eta = \frac{\rho_0 A}{\mathrm{i}\omega}\,\frac{\mathrm{D}_0\overline{G_\phi}}{\mathrm{D}t} \quad \text{on } \Gamma,\\
&\frac{\boldsymbol{u}_0\cdot\boldsymbol{y}}{c_0^2 r}\,\frac{\mathrm{D}_0\overline{G_\phi}}{\mathrm{D}t} - \frac{\partial\overline{G_\phi}}{\partial r} = \mathrm{i}k\alpha\overline{G_\phi} \quad \text{on } \Gamma_\infty.
\end{aligned}\right\} \tag{4.1}$$

It is apparent that these equations for $\overline{G_\phi}$ are consistent with the direct problem for ϕ given in § 2.1. Hence existing solvers for the direct problem can be reused directly for the adjoint problem by solving for the complex conjugate of the adjoint Green's function and by reversing the mean flow direction. This so-called flow reversal theorem allows us to relate more easily the direct and adjoint problems; see Godin (1997), Möhring (1978) and Eversman (2001*b*).

For Pierce's equation, the governing equations (3.1), (3.6) and (2.16) for the tailored adjoint Green's function H_φ become

$$\left.\begin{aligned}
&\boldsymbol{\nabla}\cdot\left(\frac{1}{\rho_0}\boldsymbol{\nabla}\overline{H_\varphi}\right)-\rho_0\frac{\mathrm{D}_0}{\mathrm{D}t}\left(\frac{1}{\rho_0^2c_0^2}\frac{\mathrm{D}_0\overline{H_\varphi}}{\mathrm{D}t}\right)=\delta(\boldsymbol{x}-\boldsymbol{y})\quad\text{in }\Omega,\\
&\frac{\partial\overline{H_\varphi}}{\partial n}=-\rho_0^2\left\{\frac{\mathrm{D}_0\bar{v}}{\mathrm{D}t}-\bar{v}\boldsymbol{n}\cdot[(\boldsymbol{n}\cdot\boldsymbol{\nabla})\boldsymbol{u}_0]\right\}\quad\text{with }\bar{v}=\frac{A}{\mathrm{i}\omega}\frac{\mathrm{D}_0}{\mathrm{D}t}\left(\frac{\overline{H_\varphi}}{\rho_0}\right)\quad\text{on }\Gamma,\\
&\frac{\boldsymbol{u}_0\cdot\boldsymbol{y}}{c_0^2r}\frac{\mathrm{D}_0\overline{H_\varphi}}{\mathrm{D}t}-\frac{\partial\overline{H_\varphi}}{\partial r}=\mathrm{i}k\alpha\overline{H_\varphi}\quad\text{on }\Gamma_\infty.
\end{aligned}\right\}\tag{4.2}$$

It can be noted that the governing equation and the radiation condition are identical to the direct problem for φ; see (3.1) and (2.16). However, the impedance condition differs from that of the direct problem (3.6), except in the case of an incompressible base flow.

The variational form for the system (4.2) reads

$$\begin{aligned}
&\int_\Omega\frac{1}{\rho_0}\left(\frac{1}{c_0^2}\frac{\mathrm{D}_0\overline{H_\varphi}}{\mathrm{D}t}\frac{\overline{\mathrm{D}_0\psi}}{\mathrm{D}t}-\boldsymbol{\nabla}\overline{H_\varphi}\cdot\boldsymbol{\nabla}\bar{\psi}\right)\mathrm{d}\Omega\\
&\quad-\int_{\partial\Omega}\frac{\bar{\psi}}{\rho_0}\left(\frac{\boldsymbol{u}_0\cdot\boldsymbol{n}}{c_0^2}\frac{D_0\overline{H_\varphi}}{\mathrm{D}t}-\frac{\partial\overline{H_\varphi}}{\partial n}\right)\mathrm{d}\Gamma=\int_\Omega\bar{\psi}\delta(\boldsymbol{x}-\boldsymbol{y})\,\mathrm{d}\Omega.
\end{aligned}\tag{4.3}$$

The contribution of the impedance condition to the boundary integral is

$$I_\Gamma=\int_\Gamma\frac{\rho_0A}{\mathrm{i}\omega}\frac{\mathrm{D}_0}{\mathrm{D}t}\left(\frac{\overline{H_\varphi}}{\rho_0}\right)\frac{\overline{\mathrm{D}_0\psi}}{\mathrm{D}t}\,\mathrm{d}\Gamma.\tag{4.4}$$

4.2. *High-order finite element model*

We use a high-order continuous Galerkin finite element method (FEM) equipped with a basis of integrated Legendre polynomials to discretise the weak formulations of the direct and adjoint problems. In Bériot *et al.* (2016), this approach was shown to provide substantial reductions in memory and CPU time when compared to conventional finite elements for acoustic applications. The benefits of a high-order FEM (e.g. low dispersion error, exponential convergence for smooth solutions) are also retained in the presence of background mean flows (Bériot, Gabard & Perrey-Debain 2013). In the numerical simulations, it is helpful to maintain an equivalent discretisation accuracy when varying the frequency or the Mach number. We resort to the *a priori* error indicator proposed in Bériot & Gabard (2019), which adjusts the order across the mesh so as to achieve a given, user-defined L^2-error target accuracy E_T. In practice, the edge orders are first determined based on a one-dimensional error indicator, which accounts for the local in-flow dispersion relation properties and possible edge curvature. In a second step, the

element interior (directional) orders are assigned through a set of simple element-based dependent conformity rules. The orders are here defined to be in the range $p_{FEM} \in [1, 10]$.

The governing equations of the direct and adjoint problems contain singular source terms, which require special attention. In practice, the point sources are enforced directly using a Dirac in the weak form. Error estimates have been derived in the literature for such elliptic problems with singular right-hand sides; see, for instance, Bertoluzza *et al.* (2018). They indicate that the preponderant part of the error is located in the close vicinity around the source. A usual recommendation is therefore to use graded meshes, so as to confine the singularity errors in a more compact region. However, mesh refinements increase model complexity and may become unwieldy when several Dirac source terms are present. In Koppl & Wohlmuth (2014), it is shown that the optimal convergence of high-order finite elements is recovered without mesh grading, if one excludes the one-ring neighbourhood elements to the point source from the error evaluation. In practice, one is usually not interested in getting a very accurate solution in the few elements directly surrounding the singularity. As a result, in this study, no mesh refinement is applied around the source when computing the tailored adjoint Green's functions.

4.3. *Acoustic transfer vectors*

Once discretised, the explicit expression (2.31) for the solution ϕ can be written as scalar products between complex-valued vectors:

$$\phi(\boldsymbol{x}) = \boldsymbol{a}_\phi^{\mathrm{T}}(\boldsymbol{x})\, \boldsymbol{v}_s + \boldsymbol{b}_\phi^{\mathrm{T}}(\boldsymbol{x})\, \boldsymbol{q}, \tag{4.5}$$

where $^{\mathrm{T}}$ denotes the Hermitian transpose. A similar expression can be written for φ using (3.14). The vectors $\boldsymbol{v}_s$ and $\boldsymbol{q}$ contain the degrees of freedom representing the source terms v_s and q on the finite element mesh. The vectors $\boldsymbol{a}_\phi$ and $\boldsymbol{b}_\phi$ can be identified easily from (2.31) and computed using the solution for G_ϕ. These vectors are sometimes referred to as acoustic transfer vectors as they act as transfer functions between the distributed sources v_s and q and the solution observed at a point $\boldsymbol{x}$ (Tournour *et al.* 2000). These vectors are particularly useful when considering large numbers of different source distributions. For each individual source distribution, the new solution ϕ can be calculated very rapidly using (4.5) (a scalar product has linear complexity with respect to the number of degrees of freedom involved).

Additionally, when dealing with stochastic sources, acoustic transfer vectors can greatly simplify the computation of the acoustic field properties. For instance, for the volume source q, one can write

$$\mathbb{E}[\phi\bar{\phi}] = \boldsymbol{b}_\phi^{\mathrm{T}}\, \mathbb{E}[\boldsymbol{q}\boldsymbol{q}^{\mathrm{T}}]\, \boldsymbol{b}_\phi, \tag{4.6}$$

where $\mathbb{E}$ denotes the expected value. The correlation matrix $\mathbb{E}[\boldsymbol{q}\boldsymbol{q}^{\mathrm{T}}]$ can be either calculated or modelled, depending on the nature of the source mechanism. From this correlation matrix, the sound field can be computed directly using the acoustic transfer vector $\boldsymbol{b}_\phi$. This approach has been used extensively to predict aerodynamic noise generation by turbulent flows, starting from Tam & Auriault (1999). See Spieser (2020) for a comprehensive literature review on this approach.

It is important to note the presence of the gradient of G_ϕ in the definition of the vector $\boldsymbol{a}_\phi$. The gradient can be evaluated directly from the finite element approximation of G_ϕ obtained after solving (4.1). This can be an issue if a low-quality numerical solution is used for G_ϕ since the evaluation of $\boldsymbol{a}_\phi$ will be inaccurate.

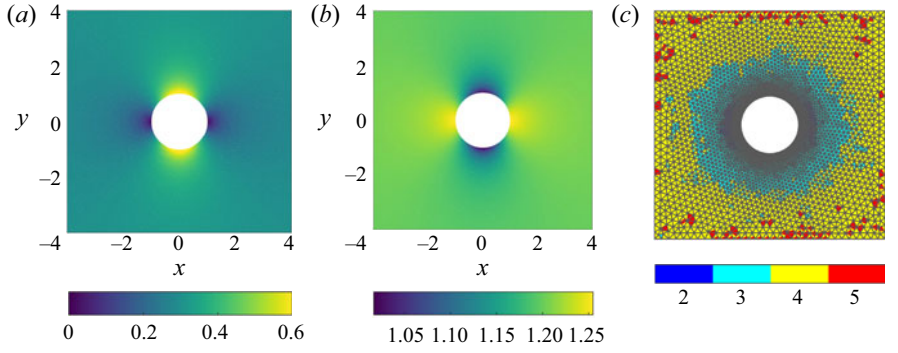

Figure 1. Computational domain: (*a*) mean Mach number, (*b*) mean density, and (*c*) mesh with FEM face order distribution for $\omega = 10c_0/R$.

An alternative approach is to integrate by parts the first integral in (2.31) to transfer the derivative onto v_s. This is similar to rewriting (2.7) into (2.10). The resulting expression is

$$\phi(\boldsymbol{x}) = \int_\Gamma \overline{G_\phi}\,\frac{\rho_0}{\mathrm{i}\omega}\,\frac{\mathrm{D}_0 v_s}{\mathrm{D}t}\,\mathrm{d}\Gamma_y - \int_\Omega \overline{G_\phi}\,q\,\mathrm{d}\Omega_y. \tag{4.7}$$

This avoids having to differentiate G_ϕ, which is computed numerically. However, if the prescribed normal velocity v_s is poorly represented, for instance with noisy data, then computing its derivative might introduce more numerical error. Depending on the application at hand, one has to choose which of these two approaches is best suited.

5. Applications

The proposed propagation models, both direct and adjoint, are now applied to several two-dimensional test cases to verify the formulation and implementation and to illustrate their applications.

5.1. *Cylinder in compressible flow*

The proposed methodology is first applied to compute the sound radiated by a point source located in the vicinity of a cylinder immersed in a steady compressible flow. The computational domain consists of a square of side 8 m, represented in figure 1(*a*). The cylinder is centred at $x = y = 0$ and has radius $R = 1$ m. Far from the cylinder, the mean flow is in the positive x direction with Mach number $M_\infty = 0.3$, density $\rho_\infty = 1.2\ \mathrm{kg\ m^{-3}}$, and speed of sound $c_\infty = 340\ \mathrm{ms^{-1}}$. The flow field around the cylinder is computed using a compressible homentropic potential flow solver (hence for an inviscid, non-heat-conducting gas). The flow is then interpolated onto the acoustic mesh. The local Mach number varies up to 0.662, as illustrated in figure 1(*a*). The cylinder is treated acoustically with uniform impedance $Z = \rho_\infty c_\infty(2 - 2\mathrm{i})$ and is vibrating with surface velocity $\boldsymbol{v}(x, y) = [\cos(x), 0]^{\mathrm{T}}$. In this example, a point source $\delta(\boldsymbol{x} - \boldsymbol{x}_s)$ is placed at $x_s = -1$ m and $y_s = -2$ m, and the observer is located at $x = y = 2.5$ m.

The adjoint methods for Goldstein's and Pierce's equations are used to compute the acoustic field at the observer. Numerical simulations are performed over the normalised frequency range $1 \leqslant \omega R/c_\infty \leqslant 10$. The computational domain is discretised with 6-node triangular elements whose curved edges allow us to better represent the geometry of

the cylinder. The size of the finite elements ranges from $h = 0.05$ m on the cylinder surface to $h = 0.25$ m at the outer boundary of the domain, corresponding respectively to 12.6 and 2.5 elements per acoustic wavelength at the highest frequency of interest. This leads to approximately 6700 elements in the domain. The FEM *a priori* error indicator automatically adjusts the order of the finite element basis to the user-defined accuracy, the frequency, the mean flow and the element size distribution, also accounting for the curvature of the mesh (Bériot & Gabard 2019). The mesh is shown in figure 1(*c*) together with the distribution of polynomial orders obtained with target accuracy $E_T = 1\,\%$. The face order p_{FEM} varies from 2 to 5 at $\omega = 10c_\infty/R$. At the outer boundaries, perfectly matched layer (PML) regions made of ten layers are extruded automatically to absorb outgoing waves (Bériot & Modave 2021). They are stabilised using Lorentz transformation, following the work in Marchner *et al.* (2021).

Figure 2 presents the results obtained for the direct and adjoint problems at $\omega = 10c_\infty/R$ using Goldstein's equation. The real parts of the acoustic potential and pressure fields obtained for the direct problem are shown in figures 2(*a*) and 2(*b*), respectively. The sound field radiated from the source is clearly visible and is scattered by the cylinder, which also radiates sound due to its surface vibration. Also visible is the mean flow effect on the sound waves, with shorter waves propagating upstream, and longer waves propagating downstream. Figures 2(*c*) and 2(*d*) show the solutions G_ϕ and G_p of the adjoint problem. In these solutions, waves are converging towards the observer location (these waves are anti-causal) and are scattered by the cylinder. Due to the flow reversal theorem, shorter wavelengths are observed on the right and longer wavelengths on the left, which is the opposite of the direct solutions.

The solutions of the direct problems based on Goldstein's and Pierce's equations are now compared to those obtained with the tailored adjoint Green's functions G_ϕ, G_p or H_φ, using (2.31), (2.33) or (3.14). Figure 3 shows the variables $\phi(\boldsymbol{x})$, $\varphi(\boldsymbol{x})$ and $p(\boldsymbol{x})$ computed at the observer location for a range of frequencies $1 \leqslant \omega R/c_\infty \leqslant 10$. For Goldstein's equation, the potential and pressure fields calculated with the adjoint approach and (2.31) and (2.33) match exactly the solutions of the direct problem. The same conclusion is obtained for Pierce's equation. These results demonstrate the applicability of the adjoint method to compressible non-parallel flows, in the presence of lined and vibrating surfaces.

For this test case, the assumptions of Goldstein's equation (homentropic and irrotational mean flow) are all valid, and this equation thus provides the reference solution. Note that the mean flow is not exactly isothermal since the mean temperature varies slightly around the cylinder (these variations do not exceed a few per cent). As a consequence, the mean density and sound speed also vary; see figure 1(*b*). In this case, Pierce's equation is approximate but still provides results in excellent agreement with Goldstein's equation (see figure 3*c*). It is only at low frequency ($\omega R/c_\infty \simeq 1$) that very small discrepancies can be observed between the two propagation equations. These discrepancies can be attributed to the small gradients of ρ_0 and c_0, and the high-frequency assumption used in Pierce's equation. In § 5.3, we will illustrate the differences between these wave equations when significant mean temperature gradients are present.

5.2. *Sound source in a lined duct with flow*

The second application involves a point source located in a two-dimensional straight duct with a uniform flow and a finite lined section modelled using the Myers impedance condition. The aim is to validate the formulation of the adjoint Myers condition for Goldstein's equation as well as the proposed formulations for the direct and adjoint Myers condition for Pierce's equation. These formulations, described in §§ 2 and 3, involve the

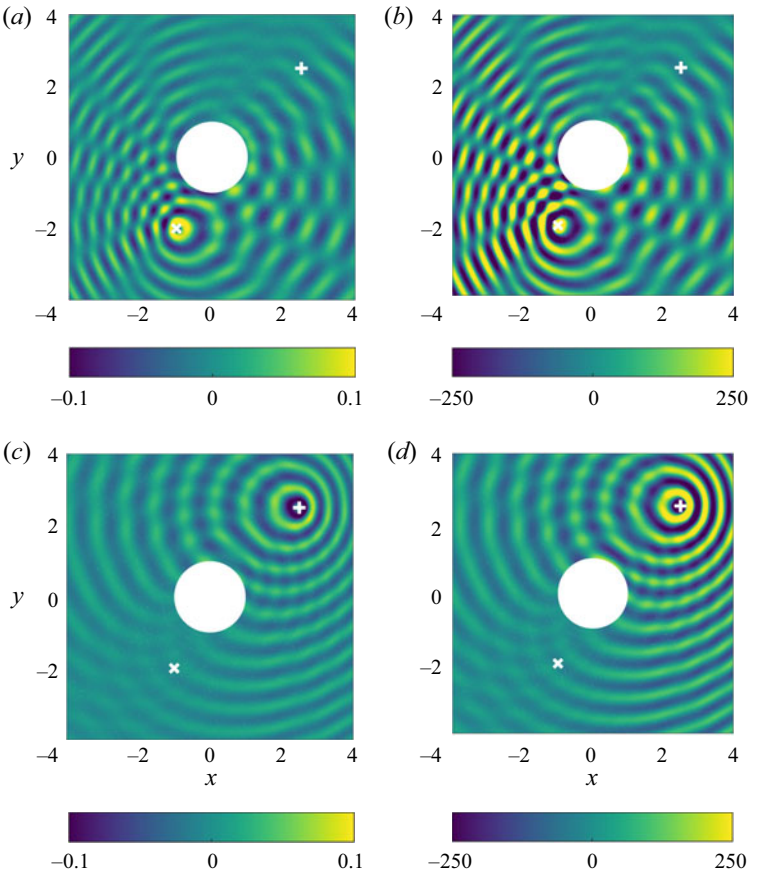

Figure 2. Real parts of (*a*) the acoustic potential and (*b*) the pressure obtained with the direct problem for Goldstein's equation. Real parts of the numerical Green's functions (*c*) G_ϕ and (*d*) G_p obtained from the corresponding adjoint problem, at $\omega = 10c_\infty/R$. Symbol $\times$ indicates source location, and $+$ indicates observer position.

neglect of contour terms around the lined surfaces, which could not be validated in the previous test case.

The straight duct, shown in figure 4(*a*), has height $h_d = 0.2$ m and length $r_d = 0.75$ m. Inside the duct, the uniform flow is such that $\rho_0 = 1.225$ kg m^{-3}, $c_0 = 340$ m s^{-1} and $M_0 = u_0/c_0 = 0.5$. On the duct upper wall, uniform surface impedance $Z = \rho_0 c_0(2 - 2\mathrm{i})$ is defined for $0.125 < x < 0.625$ m. The point source, placed at $x_s = 0.25$ m and $y_s = 0.1$ m, is defined as $10^{-3}\delta(\boldsymbol{x} - \boldsymbol{x}_s)$. The acoustic potential and pressure fields are computed at the observer position $x = 0.6$ m and $y = 0.1$ m.

The finite element simulations are performed for frequency $f = 5$ kHz and target accuracy $E_T = 1\,\%$. The mesh of triangular elements is shown in figure 4(*b*) together with the distribution of face orders. The size of the elements inside the duct varies from $h = 0.0025$ m at the wall to $h = 0.025$ m at the centre of the duct. The face order p_{FEM} varies between 1 and 5. In order to absorb outgoing waves, PML regions made of 10 layers are introduced at the duct terminations.

Acoustic results obtained using Goldstein's equation are presented in figure 5. For the direct problem, the real part of the acoustic potential and pressure are given in figures 5(*a*)

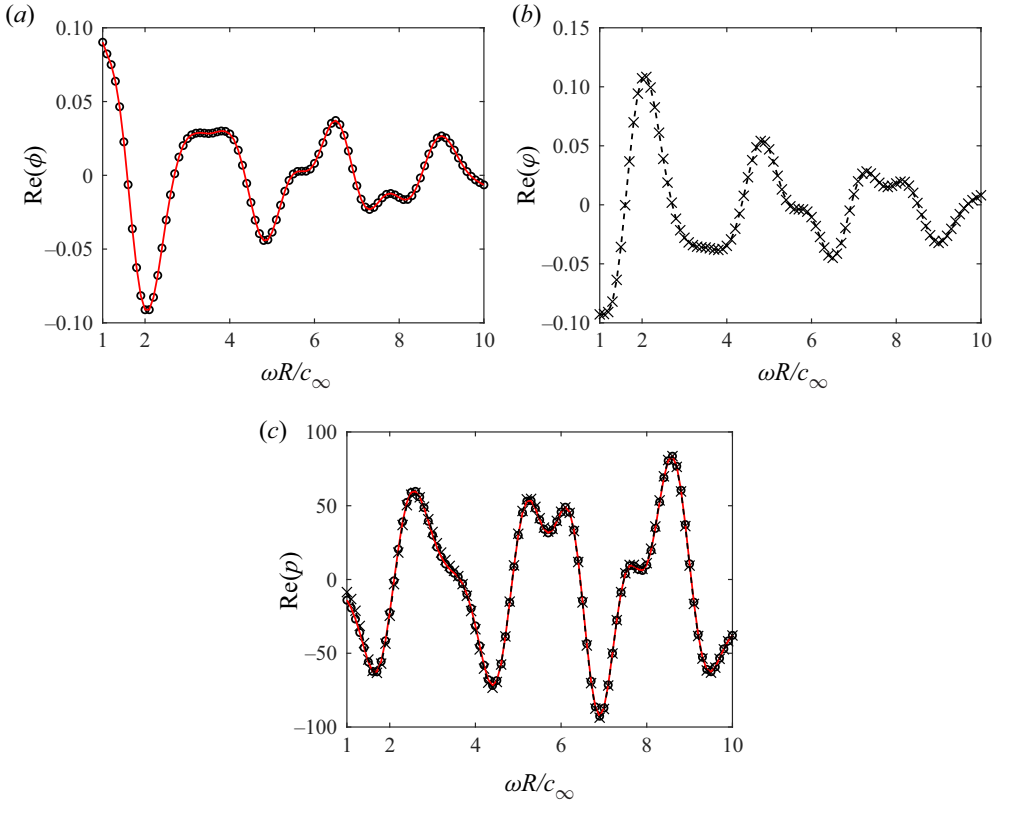

Figure 3. Real parts of (*a*) the acoustic potential ϕ, (*b*) the acoustic potential φ, and (*c*) the acoustic pressure computed at $x = y = 2.5R$. Here, ○ indicates Goldstein's direct problem, × indicates Pierce's direct problem, red solid line indicates Goldstein's adjoint problem, and dashed line indicates Pierce's adjoint problem.

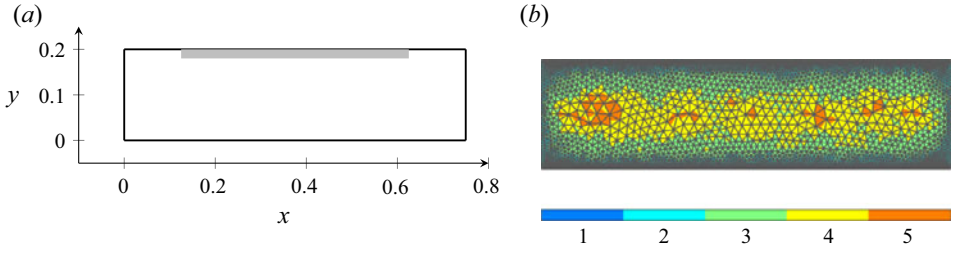

Figure 4. (*a*) Computational domain with liner in grey. (*b*) Mesh with FEM face order distribution at $f = 5$ kHz.

and 5(*b*), respectively. For the adjoint problem, the real part of the numerical Green's functions G_ϕ and G_p are shown in figures 5(*c*) and 5(*d*). As for the previous test case, the Green's functions G_ϕ and G_p exhibit waves converging towards the observer position, and the effect of the mean flow on the wavelength is reversed when compared to the direct problem. Using these tailored adjoint Green's functions together with (2.31) and (2.33) yields solutions for ϕ and p at the observer location in figure 5 that are identical to the solutions of the direct problem within floating-point precision. The results obtained with

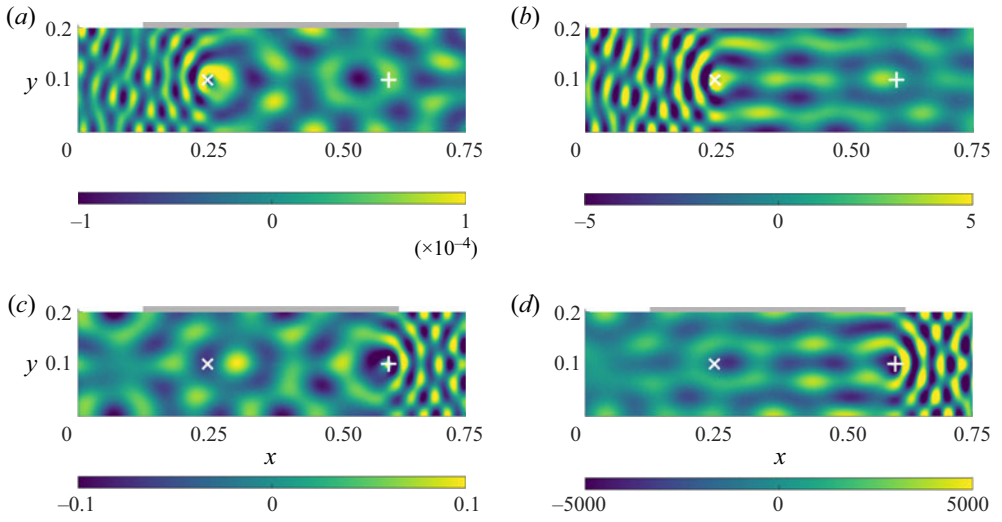

Figure 5. Real parts of (*a*) the acoustic potential and (*b*) the pressure field obtained for Goldstein's equation, and real parts of the corresponding numerical Green's functions (*c*) G_ϕ and (*d*) G_p obtained from the adjoint problem at $f = 5$ kHz. Symbol $\times$ indicates source location, and $+$ indicates observer location. The liner is indicated in grey.

Pierce's equation are not shown here for the sake of brevity since they are identical to those in figure 5. This is because, with a uniform mean flow, the wave operators in (2.1) and (3.1) are equivalent since dividing the former by ρ_0^2 yields the latter.

To verify further the proposed models, they are compared to the semi-analytical mode-matching model from Gabard (2010). The three solutions along the upper duct wall are compared in figure 6. Again, the solutions from Goldstein's and Pierce's equations are identical. They are also in close agreement with the mode-matching solution, even in the vicinity of the impedance discontinuities at $x = 0.125$ and 0.625, where the acoustic pressure varies rapidly. The velocity potentials ϕ and φ vary continuously in these regions, but their slopes change across the impedance discontinuities. This behaviour is well resolved by the high-order finite element method. The pressure fields shown in figure 6 are obtained by computing $p = -\rho_0 \mathrm{D}_0\phi/\mathrm{D}t$ or $p = \mathrm{D}_0\varphi/\mathrm{D}t$. It is the gradient $\boldsymbol{u}_0 \cdot \nabla$ included in the material derivative that results in rapid variations of p near impedance discontinuities. This behaviour is well-known and expected; see Gabard (2010) and Luneville & Mercier (2014) for more details.

These results confirm that the formulation of the adjoint Myers condition for Goldstein's equation proposed in § 2.2.2 is consistent with the standard formulation of Eversman (2001*a*). This also confirms that the formulations of the direct and adjoint Myers impedance conditions for Pierce's equation proposed in § 3 are consistent with those for Goldstein's equation.

5.3. *Propagation in sheared non-isothermal flows*

In the results presented above, Pierce's and Goldstein's wave equations yield almost identical results. This is not always the case, in particular when the mean flow includes strong temperature gradients. To illustrate this, two additional test cases are considered, namely the sound radiated by a source in a hot jet, and the sound produced by a point source in a duct with a hot sheared flow. The solutions from the direct problems are

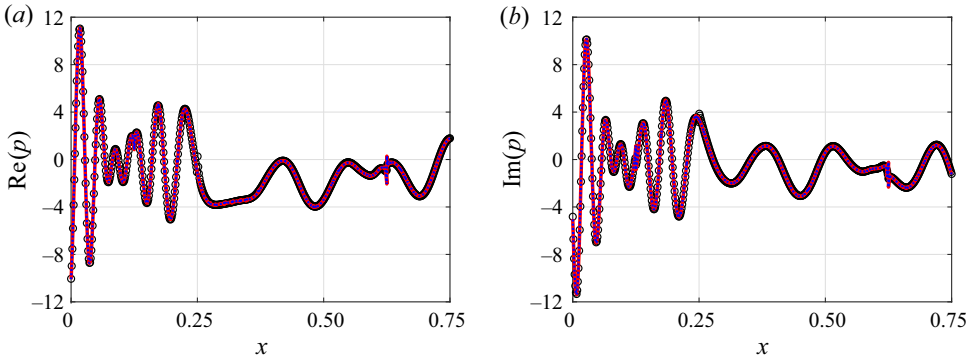

Figure 6. (*a*) Real part and (*b*) imaginary part of the pressure field at $f = 5$ kHz along the lined duct top wall ($y = h_d$). Here, blue dashed line indicates Pierce's equation, red solid line indicates Goldstein's equation, and ○ indicates mode-matching results (reference).

also compared to reference solutions obtained with the linearised Euler equations solved using the same high-order finite element method (Hamiche *et al.* 2019). The aim is to assess quantitatively the impact of the simplifications involved in Pierce's and Goldstein's operators when mean temperature gradients are present or when the mean flow is not homentropic.

Adjoint problems have also been computed and lead to the same results as the direct problems. For the sake of brevity, adjoint results have not been included in this subsection.

5.3.1. *Free-field propagation*

The case of a localised heat source radiating in a hot jet flow corresponds to the benchmark problem used in Spieser (2020), except that two-dimensional calculations are performed instead of axisymmetric ones. The base flow is based on the fourth CAA workshop; see section 'Radiation and refraction of sound waves through a two-dimensional shear layer' of Dahl (2004). The mean flow is parallel along the x axis with a velocity profile defined as

$$u_0(y) = u_j \exp\left(-\frac{y^2}{2\sigma^2}\right), \tag{5.1}$$

where $\sigma = 1.1018$ m, $u_j = M_j c_j$, $c_j = \sqrt{\gamma R T_j}$, $T_j = 600$ K, $\gamma = 1.4$ and $R = 287$ m^2 s^{-2} K^{-1}. The mean density is defined using the Crocco–Busemann law:

$$\frac{\rho_j}{\rho_0(y)} = \frac{T_\infty}{T_j} - \left(\frac{T_\infty}{T_j} - 1\right)\frac{u_0(y)}{u_j} + \frac{\gamma - 1}{2} M_j^2 \frac{u_0(y)}{u_j}\left(1 - \frac{u_0(y)}{u_j}\right), \tag{5.2}$$

where $T_\infty = 300$ K and $\rho_j = \sqrt{\gamma p_0 / c_j^2}$, with $p_0 = 103\,330$ Pa. The jet flow Mach number is set to $M_j = 0.9$. Note that this mean flow is isentropic but not homentropic. Following Dahl (2004), the sound source is defined as a source term in the energy equation of the LEE written for the variables $[\rho', \rho_0 \boldsymbol{u}', p']^{\mathrm{T}}$. The source distribution is

$$q_p(x, y) = \sigma_s \sqrt{e} \exp\left(-\frac{x^2 + y^2}{2\sigma_s^2}\right), \tag{5.3}$$

with $\sigma_s = 0.136\sigma$. Corresponding source terms are derived for Goldstein's and Pierce's equations.

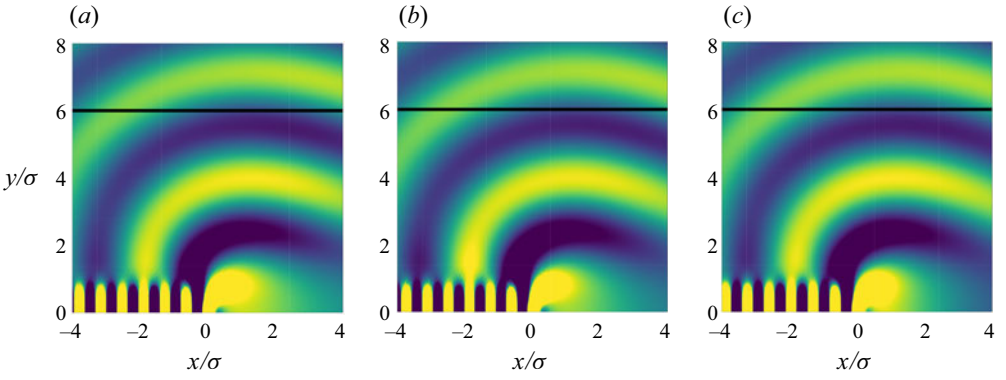

Figure 7. Real part of the pressure field for the hot jet problem at $St = 0.5$ obtained with (*a*) Goldstein's equation, (*b*) Pierce's equation, and (*c*) the LEE. Levels between -10^{-5}Pa and 10^{-5} Pa from blue to yellow.

The computational domain extends from -5σ to 18σ in the x direction, and from -3σ to 9σ in the y direction, with the jet centreline at $y = 0$. At the external boundaries, a PML region of thickness 2σ and made of five layers is used to absorb outgoing waves. Simulations are performed for Strouhal numbers $St = 2\sigma f/u_j$ in the range $0.5 \leqslant St \leqslant 3$.

A triangular mesh is used for the finite element solution. The element size is $h = \sigma/30$ along the jet centreline to discretise the point source and the jet shear layers. It is increased progressively to reach $h = 0.6\sigma$ at the external boundaries of the domain. For the FEM simulations, the target error for the *a priori* error estimator is set to 1 %, resulting in FEM polynomial orders varying between 1 and 8.

The real part of the pressure field computed with Goldstein's, Pierce's and the LEE operators at $S_t = 0.5$ is shown in figure 7. The real part of the pressure field obtained along the line $y = 6\sigma$ is shown in figure 8(*a*). Some differences can be observed between the three models, especially downstream of the source. Pierce's equation follows more closely the LEE compared to Goldstein's equation. This is confirmed by computing a relative error with respect to the LEE solution as a function of frequency from the pressure field at $y = 6\sigma$. Results are presented in figure 8(*b*). Results from Goldstein's equation are consistently less accurate than with Pierce's equation. Also significant in figure 8(*b*) is the decrease of the relative error as the frequency increases, which is consistent with the high-frequency analysis used by Pierce (1990). This is explained by the fact that the assumptions needed for Goldstein's equation are not satisfied: the mean flow is neither homentropic nor irrotational. Pierce's equation does not need these assumptions, but relies instead on a high-frequency approximation.

Table 1 compares the computational costs of the different wave operators in terms of number of degrees of freedom (DoF), memory footprint and solving time. For a given mesh and accuracy, the use of the LEE leads to an increase by a factor 7 in the execution time and by a factor 15 in the memory requirements of the linear solver when compared to Pierce's or Goldstein's equations. This is consistent with the comparison for three-dimensional calculations reported by Hamiche *et al.* (2019).

For completeness, figure 8(*b*) also includes results for the same case but with uniform temperature $T_0 = 600$ K. In this case, ρ_0 and c_0 are uniform, hence Goldstein's and Pierce's equations are equivalent, which is confirmed by figure 8(*b*). The accuracy of Goldstein's equation is improved significantly compared to the non-isothermal-jet case because the mean flow is now homentropic. The remaining error compared to the LEE is

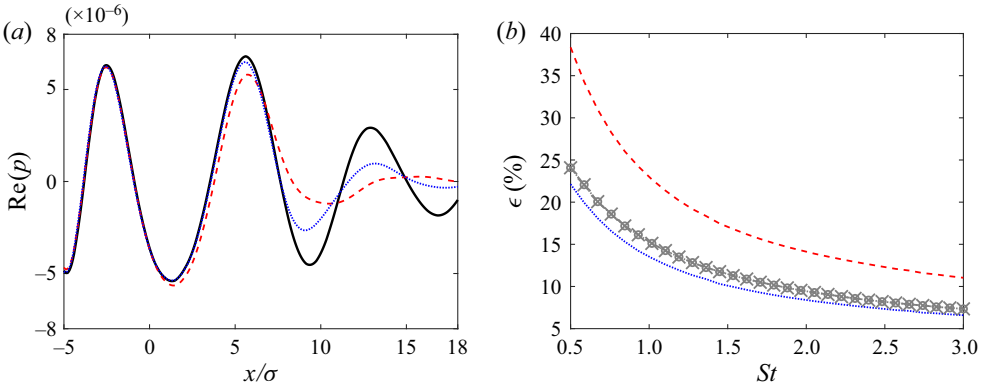

Figure 8. (*a*) Real part of the acoustic pressure at $y = 6\sigma$ for $St = 0.5$, and (*b*) corresponding relative error ϵ (with LEE as reference) for an increasing Strouhal number. Here, solid line indicates LEE, blue dotted line indicates Pierce's equation, and red dashed line indicates Goldstein's equation. Error levels for an isothermal jet with $T_0 = 600$ K are also reported: × indicates Pierce's equation, and ○ indicates Goldstein's equation.

Method	Number of DoF	Factorisation memory (Mb)	Solving time (s)
Goldstein	270 300	723	4
Pierce	270 300	723	4
LEE	1 081 100	10 900	28

Table 1. Comparison of the computational costs of the different wave operators as reported by the MUMPS linear solver (Amestoy *et al.* 2001), for the non-isothermal jet flow problem at $St = 3$.

due to the jet flow, which contradicts the irrotational flow assumption used for Goldstein's equation.

5.3.2. *In-duct propagation*

In this test case, a point mass source is located in a duct containing a hot sheared flow. The definitions of the duct and the source are identical to those of the duct problem presented in § 5.2, except that no liner is considered. Inside the duct, a mean velocity profile is defined as

$$u_0(y) = u_j \left(1 - \left|1 - \frac{2y}{h_d}\right|^n\right), \tag{5.4}$$

with $n = 3$, $T_j = 600$ K, $\gamma = 1.4$ and $R = 287\text{m}^2\ \text{s}^{-2}\ \text{K}^{-1}$. The flow Mach number along the duct centreline is $M_j = 0.5$. The mean density is defined from the Crocco–Busemann law (5.2) with $T_\infty = 300$ K and $p_0 = 103\,330$ Pa.

The direct problems based on either Pierce's or Goldstein's operator are solved with the high-order FEM method, and the results are compared to the LEE solutions. All the numerical simulations are carried out with $f = 5$ kHz using a mesh similar to that used in § 5.2. The *a priori* accuracy target is $E_T = 1\,\%$, resulting in polynomial orders p_{FEM} varying between 1 and 4.

The acoustic pressure in the duct computed from the three linearised operators is shown in figure 9. While the overall pressure distributions are similar between the three

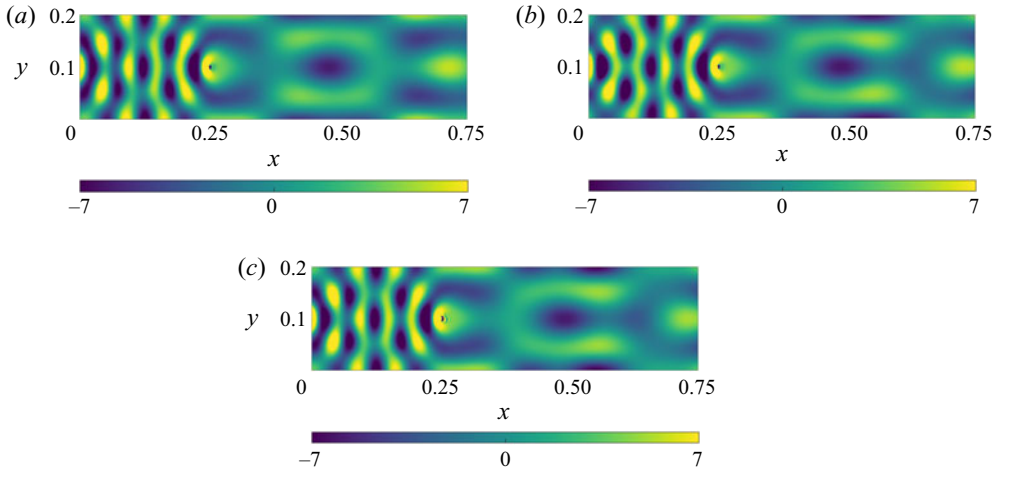

Figure 9. Real part of pressure in the duct with sheared flow at $f = 5$ kHz, for (a) Goldstein's equation, (b) Pierce's equation, and (c) the LEE. Levels between -7 Pa and $+7$ Pa from blue to yellow.

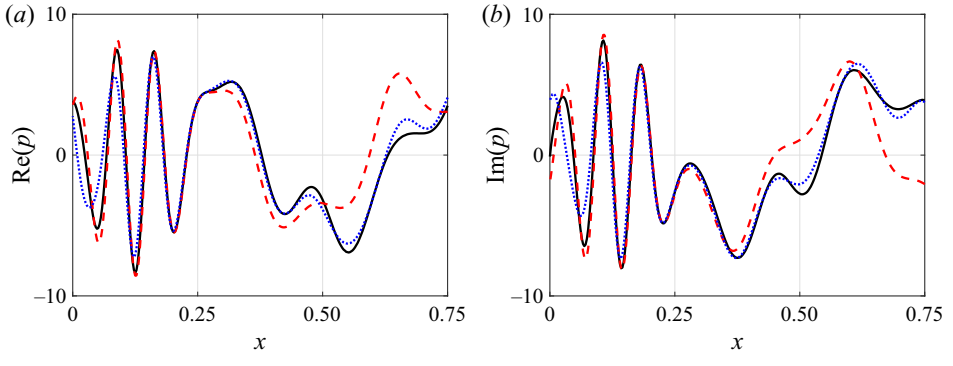

Figure 10. (a) Real part and (b) imaginary part of the pressure field at $f = 5$ kHz along the duct top wall ($y = h_d$), Here, solid line indicates the LEE, blue dotted line indicates Pierce's equation, and red dashed line indicates Goldstein's equation.

solutions, the details of the solution obtained with Pierce's equation follow more closely the reference solution.

The real and imaginary parts of the acoustic pressure along the duct top wall are shown in figure 10 for the three propagation operators. The best agreement with the LEE reference solution is clearly obtained with Pierce's equation. The relative error with respect to the LEE solution is 26.1 % using Pierce's equation and 52.3 % using Goldstein's equation. The variation of the relative error from the LEE solution is shown in figure 11 for a range of Helmholtz numbers $\omega h_d/c_j$ varying between 5 and 40. The same trend is observed where Pierce's equation is consistently more accurate than Goldstein's equation. These results indicate that Pierce's operator is more accurate when modelling acoustic propagation in regions with mean temperature gradients. Note that the peaks of error seen in figure 11 are due to the cut-off frequencies of the duct modes. Whenever the frequency of interest is close to the cut-off frequency of a duct mode, the models are very sensitive to any numerical error, and large discrepancies can be observed between different propagation models. This is discussed in more detail in § V.B. in Gabard (2014).

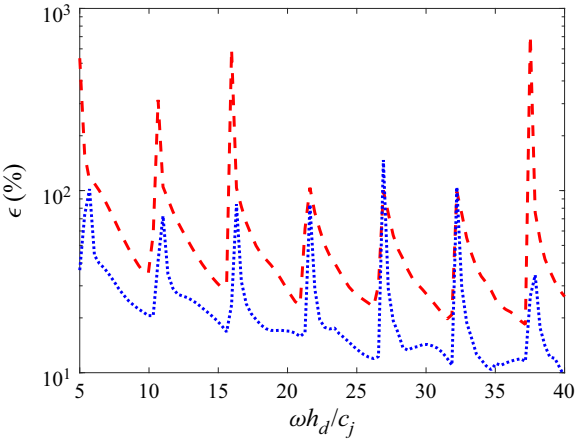

Figure 11. Relative error with respect to the LEE solution for the acoustic pressure along the duct top wall ($y = h_d$). Here, blue dotted line indicates Pierce's equation, and red dashed line indicates Goldstein's equation.

6. Summary and conclusions

In this paper, we have formulated a number of direct and adjoint problems for sound propagation with flow. The scalar wave equations from Goldstein and Pierce have been considered in a general setting, i.e. with a compressible mean flow, far-field radiation, volume sources and lined and/or vibrating surfaces. The adjoint problems have been devised to provide tailored Green's functions that facilitate the computation of the direct problem solution. While the two propagation operators considered here are self-adjoint, the various boundary conditions are not self-adjoint. In particular, the adjoint Myers impedance condition has been formulated for each propagation operator. This has been done in a manner consistent with the formulation proposed by Eversman (2001*a*) for the direct Myers condition for Goldstein's equation. The inclusion in the variational formulations of the far-field radiation condition with flow has also been revisited. By reversing the flow, the adjoint problems for the tailored Green's functions can be recast in forms that are solved readily using existing solvers for the direct problems. Using a series of test cases, the solutions obtained through the use of tailored adjoint Green's functions were found to be consistent with the direct problems, thus validating the formulation of the adjoint problems.

The differences between the two propagation operators have been highlighted in cases where the mean flow exhibits temperature gradients. In such cases, Pierce's equation was found to be more accurate and should be preferred when modelling sound propagation through non-isothermal flows. As expected, the accuracy of the two wave equations improves when the frequency increases.

The proposed adjoint problems and the associated tailored Green's functions can be useful in a wide range of applications, such as stochastic sound sources (e.g. aerodynamic noise sources) and source localisation problems. In addition, the systematic analysis presented could also be applied to other propagation operators, such as the acoustic perturbation equations, or to other situations such as the presence of porous materials.

Funding. The authors from Siemens gratefully acknowledge the European Commission for its support through the ENODISE project (Enabling optimized disruptive airframe-propulsion integration concepts, grant agreement no. 860103) and BPI France for its financial support through the AC-FUI25-CALMAA project

(Ciblage des Sources Aéroacoustiques par voie Logicielle et Méthodes inverses). The authors are also grateful to Dr É. Spieser and Professor C. Bailly for discussions on adjoint methods.

Declaration of interests. The authors report no conflict of interest.

Author ORCIDs.
Sophie Le Bras https://orcid.org/0000-0001-7859-2569;
Gwénaël Gabard https://orcid.org/0000-0002-1527-4261;
Hadrien Bériot https://orcid.org/0000-0001-7370-8905.

Appendix A. Two-dimensional radiation condition

To derive the radiation condition in two-dimensions for Goldstein's equation, we apply the same reasoning as for the three-dimensional condition outlined in § 2.1.4. The sound field radiated in a uniform mean flow by a generic source term q on the right-hand side of (2.1) is given by (2.12). In two dimensions, the free-field Green's function $G(\boldsymbol{x}|\boldsymbol{y})$ is defined as

$$G(\boldsymbol{x}|\boldsymbol{y}) = \frac{\mathrm{i}}{4\beta} \exp\left\{\frac{\mathrm{i}k}{\beta^2}\,(\boldsymbol{x}-\boldsymbol{y})\cdot\frac{\boldsymbol{u}_0}{c_0}\right\} H_0^{(2)}\left(\frac{k\tilde{r}}{\beta^2}\right), \tag{A1}$$

where $H_0^{(2)}$ is the zeroth-order Hankel function of the second kind. After some developments, the following result is obtained:

$$\frac{\boldsymbol{u}_0\cdot\boldsymbol{n}}{c_0^2}\frac{\mathrm{D}_0 G(\boldsymbol{x}|\boldsymbol{y})}{\mathrm{D}t} - \frac{\partial G(\boldsymbol{x}|\boldsymbol{y})}{\partial n} = k\,\frac{r}{\tilde{r}}\,\frac{H_1^{(2)}(k\tilde{r}/\beta^2)}{H_0^{(2)}(k\tilde{r}/\beta^2)}\,G(\boldsymbol{x}|\boldsymbol{y}), \tag{A2}$$

where $H_1^{(2)}$ is the first-order Hankel function of the second kind. The derivatives on the left-hand side of (A2) operate on the $\boldsymbol{x}$ coordinate. This result is exact and valid for any value of r. When the observer is in the geometric far field (i.e. $\|\boldsymbol{x}\| \gg \|\boldsymbol{y}\|$), the distance $\tilde{r}$ can be approximated by $\hat{r}$. From (2.12) and (A2), the velocity potential satisfies the following radiation condition in the geometric far field:

$$\frac{\boldsymbol{u}_0\cdot\boldsymbol{x}}{c_0^2 r}\frac{\mathrm{D}_0\phi}{\mathrm{D}t} - \frac{\partial\phi}{\partial r} = \mathrm{i}k\alpha_{2D}\phi + O\left(\frac{1}{r^{5/2}}\right), \quad \alpha_{2D} = \frac{r}{\hat{r}}\,\frac{\mathrm{H}_1^{(2)}(k\hat{r}/\beta^2)}{\mathrm{iH}_0^{(2)}(k\hat{r}/\beta^2)}, \tag{A3a,b}$$

when $r \to +\infty$. The corresponding boundary integral in the variational formulation (2.3) is written as

$$I_{\Gamma_\infty} = \int_{\Gamma_\infty} \mathrm{i}k\alpha_{2D}\rho_0\bar{\psi}\phi\,\mathrm{d}\Gamma. \tag{A4}$$

It is interesting to note that when $k\hat{r}$ is large, it is possible to show that $\alpha_{2D} \simeq (r/\hat{r})[1 + \beta^2/(2\mathrm{i}k\hat{r})]$ (for this purpose, use (10.17.6) in DLMF 2022), which is consistent with the two-dimensional far-field boundary conditions derived by Bayliss & Turkel (1982).

References

Amestoy, P.R., Duff, I.S., L'Excellent, J.-Y. & Koster, J. 2001 A fully asynchronous multifrontal solver using distributed dynamic scheduling. *SIAM J. Matrix Anal. Applics.* **23** (1), 15–41.

Astley, R.J. 2009 Numerical methods for noise propagation in moving flows, with application to turbofan engines. *Acoust. Sci. Technol.* **30** (4), 227–239.

Bayliss, A. & Turkel, E. 1982 Far field boundary conditions for compressible flows. *J. Comput. Phys.* **48** (2), 182–199.

BÉRIOT, H. & GABARD, G. 2019 Anisotropic adaptivity of the *p*-FEM for time-harmonic acoustic wave propagation. *J. Comput. Phys.* **378**, 234–256.

BÉRIOT, H., GABARD, G. & PERREY-DEBAIN, E. 2013 Analysis of high-order finite elements for convected wave propagation. *Intl J. Numer. Meth. Engng* **96** (11), 665–688.

BÉRIOT, H. & MODAVE, A. 2021 An automatic perfectly matched layer for acoustic finite element simulations in convex domains of general shape. *Intl J. Numer. Meth. Engng* **122** (5), 1239–1261.

BÉRIOT, H., PRINN, A. & GABARD, G. 2016 Efficient implementation of high-order finite elements for Helmholtz problems. *Intl J. Numer. Meth. Engng* **106** (3), 213–240.

BERTOLUZZA, S., DECOENE, A., LACOUTURE, L. & MARTIN, S. 2018 Local error estimates of the finite element method for an elliptic problem with a Dirac source term. *Numer. Meth. P. D. E.* **34** (1), 97–120.

BLOKHINTZEV, D. 1946 The propagation of sound in an inhomogeneous and moving medium I. *J. Acoust. Soc. Am.* **18** (2), 322–328.

BOGEY, C. & BAILLY, C. 2002 Three-dimensional non-reflective boundary conditions for acoustic simulations: far field formulation and validation test cases. *Acta Acust. United AC* **88** (4), 463–471.

CHAILLAT, S., COTTÉ, B., MERCIER, J.-F., SERRE, G. & TRAFNY, N. 2022 Efficient evaluation of three-dimensional Helmholtz Green's functions tailored to arbitrary rigid geometries for flow noise simulations. *J. Comput. Phys.* **452**, 110915.

DAHL, M.D. (Ed.) 2004 *Fourth Computational Aeroacoustics (CAA) Workshop on Benchmark Problems*.

DENNERY, P. & KRZYWICKI, A. 2012 *Mathematics for Physicists*. Dover.

DLMF 2022 *NIST Digital Library of Mathematical Functions*. http://dlmf.nist.gov/, Release 1.1.4 of 2022-01-15, (ed. F.W.J. Olver, A.B. Olde Daalhuis, D.W. Lozier, B.I. Schneider, R.F. Boisvert, C.W. Clark, B.R. Miller, B.V. Saunders, H.S. Cohl & M.A. McClain).

EVERSMAN, W. 2001*a* The boundary condition at an impedance wall in a non-uniform duct with potential mean flow. *J. Sound Vib.* **246** (1), 63–69.

EVERSMAN, W. 2001*b* A reverse flow theorem and acoustic reciprocity in compressible potential flows in ducts. *J. Sound Vib.* **246** (1), 71–95.

EWERT, R. & SCHRÖDER, W. 2003 Acoustic perturbation equations based on flow decomposition via source filtering. *J. Comput. Phys.* **188** (2), 365–398.

GABARD, G. 2010 Mode-matching techniques for sound propagation in lined ducts with flow. *16th AIAA/CEAS Aeroacoustics Conference*. *AIAA Paper* 2010-3940.

GABARD, G. 2014 Noise sources for duct acoustics simulations: broadband noise and tones. *AIAA J.* **52** (9), 1994–2006.

GABARD, G., BÉRIOT, H., PRINN, A. & KUCUKCOSKUN, K. 2018 Adaptive, high-order finite-element method for convected acoustics. *AIAA J.* **56** (8), 3179–3191.

GIVOLI, D. 2004 High-order local non-reflecting boundary conditions: a review. *Wave Motion* **39** (4), 319–326.

GODIN, O.A. 1997 Reciprocity and energy theorems for waves in a compressible inhomogeneous moving fluid. *Wave Motion* **25** (2), 143–167.

GOLDSTEIN, M. 1978 Unsteady vortical and entropic distortions of potential flows round arbitrary obstacles. *J. Fluid Mech.* **89** (3), 433–468.

HAMICHE, K., LE BRAS, S., GABARD, G. & BERIOT, H. 2019 Hybrid numerical model for acoustic propagation through sheared flows. *J. Sound Vib.* **463**, 114951.

HOWE, M.S. 2003 *Theory of Vortex Sound*. Cambridge University Press.

HU, F., GUO, Y. & JONES, A. 2005 On the computation and application of exact Green's function in acoustic analogy. *11th AIAA/CEAS Aeroacoustics Conference*. *AIAA Paper* 2005-2986.

KOPPL, T. & WOHLMUTH, B. 2014 Optimal *a priori* error estimates for an elliptic problem with Dirac right-hand side. *SIAM J. Numer. Anal.* **52** (4), 1753–1769.

LUNEVILLE, E. & MERCIER, J.-F. 2014 Mathematical modeling of time-harmonic aeroacoustics with a generalized impedance boundary condition. *ESAIM: Math. Model. Numer. Anal.* **48** (5), 1529–1555.

MARCHNER, P., BERIOT, H., ANTOINE, X. & GEUZAINE, C. 2021 Stable perfectly matched layers with Lorentz transformation for the convected Helmholtz equation. *J. Comput. Phys.* **433**, 110180.

MÖHRING, W. 1978 Acoustic energy flux in nonhomogeneous ducts. *J. Acoust. Soc. Am.* **64** (4), 1186–1189.

MÖHRING, W. 1999 A well posed acoustic analogy based on a moving acoustic medium. In *Aeroacoustic Workshop SWING*, pp. 1–14.

MÖHRING, W. 2001 Energy conservation, time-reversal invariance and reciprocity in ducts with flow. *J. Fluid Mech.* **431**, 223–237.

MYERS, M. 1980 On the acoustic boundary condition in the presence of flow. *J. Sound Vib.* **71** (3), 429–434.

PIERCE, A.D. 1990 Wave equation for sound in fluids with unsteady inhomogeneous flow. *J. Acoust. Soc. Am.* **87** (6), 2292–2299.

PIERCE, A.D. 2019 *Acoustics: An Introduction to its Physical Principles and Applications*. Springer.

RIENSTRA, S.W. 2007 Acoustic scattering at a hard–soft lining transition in a flow duct. *J. Engng Maths* **59** (4), 451–475.

SCHRAM, C. 2009 A boundary element extension of Curle's analogy for non-compact geometries at low-Mach numbers. *J. Sound Vib.* **322** (1–2), 264–281.

É. SPIESER 2020 Modélisation de la propagation du bruit de jet par une méthode adjointe formulée pour l'acoustique potentielle. PhD thesis, Ecole Centrale de Lyon.

SPIESER, É. & BAILLY, C. 2020 Sound propagation using an adjoint-based method. *J. Fluid Mech.* **900**, A5.

TAM, C.K. & AURIAULT, L. 1998 Mean flow refraction effects on sound radiated from localized sources in a jet. *J. Fluid Mech.* **370**, 149–174.

TAM, C.K. & AURIAULT, L. 1999 Jet mixing noise from fine-scale turbulence. *AIAA J.* **37** (2), 145–153.

TAM, C.K. & WEBB, J.C. 1993 Dispersion-relation-preserving finite difference schemes for computational acoustics. *J. Comput. Phys.* **107** (2), 262–281.

TOURNOUR, M., CREMERS, L., GUISSET, P., AUGUSZTINOVICZ, F. & MARKI, F. 2000 Inverse numerical acoustics based on acoustic transfer vectors. In *7th International Congress on Sound and Vibration*, pp. 1069–1076.